Available online at www.sciencedirect.com
ScienceDirect
Comput. Methods Appl. Mech. Engrg. 385 (2021) 114063
Computer methods in applied mechanics and engineering
www.elsevier.com/locate/cma

DP-MPM: Domain partitioning material point method for evolving multi-body thermal–mechanical contacts during dynamic fracture and fragmentation

Mian Xiao[a], Chuanqi Liu[b,*,1], WaiChing Sun[a]

[a] Department of Civil Engineering and Engineering Mechanics, Columbia University, 614 SW Mudd, New York, NY 10027, United States
[b] State Key Laboratory of Nonlinear Mechanics, Institute of Mechanics, Chinese Academy of Sciences Beijing, 100090, China

Received 22 March 2021; received in revised form 11 June 2021; accepted 17 July 2021
Available online 12 August 2021

Abstract

We propose a material point method (MPM) to model the evolving multi-body contacts due to crack growth and fragmentation of thermo-elastic bodies. By representing particle interface with an implicit function, we adopt the gradient partition techniques introduced by Homel and Herbold (2017) to identify the separation between a pair of distinct material surfaces. This treatment allows us to replicate the frictional heating of the evolving interfaces and predict the energy dissipation more precisely in the fragmentation process. By storing the temperature at material points, the resultant MPM model captures the thermal advection–diffusion in a Lagrangian frame during the fragmentation, which in return affects the structural heating and dissipation across the frictional interfaces. The resultant model is capable of replicating the crack growth and fragmentation without requiring dynamic adaptation of data structures or insertion of interface elements. A staggered algorithm is adopted to integrate the displacement and temperature sequentially. Numerical experiments are employed to validate the diffusion between the thermal contact, the multi-body contact interactions and demonstrate how these thermo-mechanical processes affect the path-dependent behaviors of the multi-body systems.

Keywords: Material point method; Multi-body contact; Fragmentation; Brittle fracture; Thermomechanics

1. Introduction

Path-dependent behaviors of particulate systems manifest from both the micro-mechanical responses within individual particles [1–4] and how these particles interact with the surrounding particles over time [5–13]. While simulations conducted via discrete/distinct element methods may update particle contact connectivity at each incremental time step, the contact laws (e.g. Herizan contact [14], linear frictional model [15]) employed in a discrete element method are highly idealized. Examples of these idealizations include assuming specific particle shapes (e.g. sphere, flat half-space), the geometry of contacts (e.g. point-wise contacts, overlapped domain), and

* Corresponding author.
E-mail address: chuanqil@imech.ac.cn (C. Liu).
[1] Former postdoctoral research scientist, Department of Civil Engineering and Engineering Mechanics, Columbia University, 614 SW Mudd, New York, NY, 10027.

https://doi.org/10.1016/j.cma.2021.114063
0045-7825/

topology (e.g. two-particle contact, neglected deformation of particles). In recent decades, many studies are dedicated to analyzing how these idealizations affect the accuracy of the predictions and propose remedies to overcome the limitations. For instance, contacts of non-spherical particles are often approximated by clustering spheres together to form regular shapes [16]. Alternatively, Boon et al. [17] and Kawamoto et al. [18] introduce implicit functions to represent the geometry of particles of different shapes.

Nevertheless, one key issue for these attempts is that the stress field inside individual particles is not available. Hence, alternative theories that are based on force or homogenized stress of individual particles proposed to idealize the damage process either as an instant splitting of individual particles (e.g. [19]), an instant debonding of prepackaged agglomerates of particles (e.g. [20]), or removal of particles [e.g. 21]. While these methods may replicate some geometrical and topological features due to grain crushing and fragmentation, the instant splitting or debonding idealization is not suitable for high-strain rate impact where the crack growth and propagation speed are important. Furthermore, since crack and damage are not only triggered simply by the magnitude of the homogenized stress of a particle but also by how strain energy stores and concentrates locally, the lack of stress and strain field within the grain in classical discrete element simulations may lead to a violation of fracture mechanics principles even in the brittle regimes.

Furthermore, the lack of rate-dependence in the breakage criteria also make those predictions not suitable for dynamic simulations where mechanics of fragmentation and damage of brittle grains can be triggered by fracture and crack branching and hence highly sensitive to loading rates [22,23], the microstructures and the spatial heterogeneity of individual particles [24]. To circumvent these limitations, previous works such as Liu and Sun [25] explored the possibility of simulating granular assembles as a multi-body contact in an implicit quasi-static regime. While path-dependent behaviors could be triggered by rearrangement of particles and the dissipation due to the frictional slip, the topological changes of the particles due to fracture, damage, and fragmentation are not considered.

The purpose of this paper is to fill this knowledge gap by proposing a material point framework suitable to model the multi-body contact thermo-mechanics of assemblies composed of brittle particles. To capture the rate-dependence and temperature-dependence of the frictional contact and fracture of the particles, we present a material point method that captures the thermo-mechanical coupling for both bulk materials and contact surfaces, incorporate the domain partitioning techniques originated from [26] to handle the continuously evolving contact geometry, and introduce constitutive laws to capture the thermal–mechanical frictional contact, damage laws, interfacial thermal conduction among particles in the finite deformation regime. Consequentially, the proposed model is a capture of replicating the dynamic fracture and fragmentation while handling the evolving contacts due to evolving geometrical and topological changes of the crushed particle assembles.

The rest of this paper is organized as follows. We will first provide a brief literature review on topics relevant to the multi-body thermal–mechanical contact problem in this Section. Section 2 then lists the presumptions and derives a set of governing equations starting from a free energy representation. Section 3 provides details on the implementation of the proposed model in the MPM. Section 4 presents numerical examples for the validation and demonstration of the capacity of the model. Concluding remarks are provided in Section 5.

1.1. Literature review on dynamic fracture simulations

To simulate the evolving contacts properly, one must replicate the deformation, fracture, and damage that trigger the topological and geometric changes of the interfaces. For high-strain-rate applications where the crack may propagate faster than the Rayleigh wave, the crack patterns are highly sensitive to the loading rate as crack branching occurs that changes how energy dissipates [24]. Furthermore, the loading rate also plays an important role in the thermal–mechanical responses of a path-dependent material. While damage, plasticity and elastic structural heating may all lead to heat, the local temperature changes and the subsequent heat transfer may also trigger different readjustment of deformation pathways and affect the macroscopic mechanical responses [27–29].

At the high-strain-rate regime, the local temperature may change near the crack tips or contact areas due to elastic/inelastic structural heating and dissipation that occurs almost adiabatically. This thermal effect could be significant enough to affect the mechanical responses, including the onset and propagation of crack(s). For instance, Nowinski [30] stated that a solid body subject to elastic deformation may heat up in a compressive region and cool down in a tensile region. It is also experimentally observed in rocks that temperature rises in the regions with intensive stress concentration and drops for stress relaxation [31,32]. Meanwhile, temperature also plays a profound role in the frictional coefficient of the contacts and affects the strength and ductility [33].

An important prerequisite to capture these thermo-mechanical coupling effects is the precise representation of the interface geometry. This can be achieved by either embedding strong discontinuity in the interpolated displacement field or via a smeared crack approach where a continuous indicator function is used to approximate the sharp discontinuity. The extended finite element method (X-FEM) and the generalized finite element method (GFEM) belong to the first strategy. These two methods are synonymous [34] and both rely on the partition-of-unity enrichment to enrich the displacement field [35]. The crack thus can propagate independently on the mesh, which overcomes the constraint of the cohesive models [36,37]. Nevertheless, for dynamic cases where crack branching may occur, the generation of the enrichment function to replicate the geometry and the integration of the residual are both non-trivial [38,39]. Even these technical issues can be resolved, modeling the fragmentation via the embedding strong discontinuity remains difficult due to the lack of established predictive theory for the onset and the mode of the crack branching [40].

Smeared crack approaches such as phase field fracture (e.g. [41–46]), nonlocal or gradient damage models [4,47,48] provide an alternative to capture the crack branching process without requiring additional criterion to predict the onset of crack branching and the additional implementation effort to embed discontinuity. This ease of implementation provides a great advantage in handling the evolving interfaces.

To handle the geometrical nonlinearity during fracture, Moutsanidis et al. [49] incorporate the phase field fracture model in a material point method (MPM). Meanwhile, Zhang et al. [50] enhance the MPM with eigenerosion [51–54] to simulate dynamic fracturing. Recently, Homel and Herbold [26] employ a damage scalar field to present the fractures in the material point method and use this scalar field to detect contacts. Nevertheless, the thermal–mechanical coupling effect on path-dependent behaviors such as crack growth, frictional slip, and thermal conduction across the interface has not yet been considered.

1.2. Literature review on computational contact thermo-mechanics

If a mode II, mode III or mixed-mode crack is propagating under compression or an existing crack is closed, then the frictional contact may introduce sufficient energy dissipation that alters the fracture patterns. For high-strain-rate applications, the dissipation due to friction may lead to a substantial amount of heat building up near the adiabatic limit and hence affect the path-dependent behaviors of the solids [46,55,56]. Meanwhile, at the low-strain-rate regime, the thermal conductance across contact boundaries must be replicated in order to capture the interplay between the fracture process and thermo-mechanical contact mechanics. In the fully coupled thermomechanical setting, the heat conductance across the contact boundary depends on the normal contact pressure, while the contact friction may also decrease as a result of temperature rise [57]. Hence, capturing both the contact conductance and normal contact pressure are of critical importance for precisely replicating the thermo-mechanical contacts. For simplicity, the linear constitutive law for pressure-dependent thermal conductance has been widely used in the literature (e.g. [57,58]). Meanwhile, Wriggers and Miehe [59] propose a more sophisticated power law to describe contact conductance. In these cases, finite element solvers are often the choice to simulate the contact thermo-mechanical problems.

Early works on the thermo-elastic contact with FEM usually implemented a node-to-segment contact algorithm, where the contact constraints are enforced via a penalty formulation [57,59,60]. In the last decade, the mortar method provides a variationally consistent way for contact discretization [61,62]. Contact algorithms with the mortar method can enforce the contact constraint exactly via a Lagrange multiplier and therefore improves accuracy as well. In addition to modeling the thermo-elastic contact in the elastic regime, more recent work, such as [63], has also formulated Nitsche's method to simulate thermal-elasto-plasticity contact problems in a finite element solver. Nevertheless, to the best knowledge of the authors, there has not yet been any attempt to resolve the thermo-mechanical contact problems with evolving interfaces due to the brittle fracture via MPM.

2. Thermo-mechanical contact mechanics with evolving contacts

This section presents the theory of the thermo-mechanical contact mechanics for simulating the path-dependent responses of multiple continuum bodies in the geometrically nonlinear regime. Sections 2.1 and 2.2 describe the constitutive laws that capture the interplay among the frictional heating, surface, and bulk conduction and the evolution of brittle damages and the evolving interfaces. The balance principles that serve as the constraints for the material point model are provided in Section 2.3. In addition, the following assumptions are made to simplify the formulation.

1. We assume the effective stress theory [cf. 64,65] is valid such that the stored elastic energy of a material point representing a representative elementary volume (REV) is related to that of a fictitious pure elastic body by a degradation function.
2. The thermo-mechanical coupling effects are addressed by introducing a coupling function influenced by both mechanical fields and thermal fields. In this sense, the free energy function consists of three parts: (1) the pure mechanical storage energy; (2) the pure thermal energy; (3) the thermo-mechanical coupling energy [66].
3. We assume the mechanical damage influences the mechanical and thermo-mechanical coupling free energy contributions but does not affect the heat capacity.
4. To calibrate the energy consumed during the fracture propagation, we assume all of the energy released in the damage evolution process is equal to the crack surface energy [67], which is reasonable for brittle fracture.

2.1. Thermoelastic constitutive framework for the bulk continuum

Here we define the constitutive law for bodies in contacts. The continuum bodies are thermally conductive and may exhibit damage and degradation. Based on the effective stress theory, we assume that the constitutive responses of the materials in the bodies can be characterized by applying a degradation function to the hyperelastic energy functional of a fictitious material that exhibits no damage. As such, the corresponding free energy function per unit mass ψ can be decomposed into three components, i.e.,

$$\psi(\boldsymbol{b}, d, \theta) = \psi^e(\boldsymbol{b}, d) + M(J, d, \theta) + \psi^t(\theta), \tag{1}$$

where $\boldsymbol{b} = \boldsymbol{F}\boldsymbol{F}^T$ is the left Cauchy–Green strain tensor, d is the scalar damage, θ is the temperature, and $J = \det \boldsymbol{F}$ is the determinant of $\boldsymbol{F}$. As such, $\psi^e(\boldsymbol{b}, d)$ is the mechanical contribution, $M(J, d, \theta)$ is the thermo-mechanical coupling term, and $\psi^t(\theta)$ is the thermal contribution (see also [68,69]). Following Simo and Miehe [66], the expressions for these terms are:

$$\rho_o \psi^e(\boldsymbol{b}, d) = (1 - d)(U(J) + W(\boldsymbol{b}_{\text{iso}})), \tag{2}$$

$$\rho_o M(J, d, \theta) = -3(1 - d)\alpha_t(\theta - \theta_0)\frac{\partial U}{\partial J}, \tag{3}$$

$$\psi^t(\theta) = c\left[(\theta - \theta_0) - \theta \log(\theta/\theta_0)\right], \tag{4}$$

respectively, where ρ_o is the mass density on the unit reference volume, $\boldsymbol{b}_{\text{iso}} = J^{-2/3}\boldsymbol{b}$ represents the isochoric part of the left Cauchy–Green strain tensor $\boldsymbol{b}$, $U(J)$ is the volumetric part of the elastic stored energy, $W(\boldsymbol{b}_{\text{iso}})$ is the isochoric counterpart of the undamaged material, α_t is the thermal expansion coefficient, c is the heat capacity per mass, and θ_0 is the reference temperature. The energy contributions of the damaged real material (ψ^e and M) and those of the undamaged fictitious material ($\overline{\psi}^e$ and $\overline{M}$) are related by the degradation term $(1 - d)$, i.e.,

$$\psi^e(\boldsymbol{b}, d) = (1 - d)\overline{\psi}^e(\boldsymbol{b}), \quad M(J, d, \theta) = (1 - d)\overline{M}(J, \theta), \tag{5}$$

where $\rho_o\overline{\psi}^e = U(J) + \overline{W}(\bar{\boldsymbol{b}})$ indicates the undamaged storage energy on the unit reference volume only depending on deformation [70], $\rho_o\overline{M}(J, \theta) = -3\alpha_t(\theta - \theta_0)\frac{\partial U}{\partial J}$ indicates the undamaged thermo-coupling energy component on the unit reference volume.

The Kirchhoff stress $\boldsymbol{\tau}$, the entropy η and the storage energy release Y on the unit reference volume corresponding to the free energy read [71],

$$\boldsymbol{\tau} = 2\rho_o\frac{\partial \psi}{\partial \boldsymbol{b}}\boldsymbol{b}, \quad \eta = -\frac{\partial \psi}{\partial \theta}, \quad Y = -\rho_o\frac{\partial \psi}{\partial d}. \tag{6}$$

We also extract the damage multiplier as what (5) does:

$$\boldsymbol{\tau} = (1 - d)\overline{\boldsymbol{\tau}}, \quad \overline{\boldsymbol{\tau}} := 2\rho_o\left(\frac{\partial \overline{\psi}^e}{\partial \boldsymbol{b}} + \frac{\partial \overline{M}}{\partial \boldsymbol{b}}\right)\boldsymbol{b}, \tag{7}$$

where $\overline{\boldsymbol{\tau}}$ is called the effective Kirchhoff stress in continuum damage mechanics [72]. This extraction is helpful since $\overline{\boldsymbol{\tau}}$ indicates the Kirchhoff stress without mechanical damage softening.

2.2. Thermal-sensitive frictional constitutive framework for contacts

Consider a contact between two distinct bodies. The Karush–Kuhn–Tucker (KKT) conditions for the normal and tangential contact on the contact boundary Γ_c reads [25,58]:

$$p_{cn} < 0, \quad \delta_n > 0, \quad p_{cn}\delta_n = 0. \tag{8}$$

$$|p_{ct}| \le \mu_c |p_{cn}|, \quad \begin{cases} \dot{\delta}_t = 0 \text{ for } |p_{ct}| < \mu_c |p_{cn}|, \\ |\dot{\delta}_t| \ge 0 \text{ for } |p_{ct}| = \mu_c |p_{cn}|. \end{cases} \tag{9}$$

where $p_{cn} \coloneqq \boldsymbol{p}_c \cdot \boldsymbol{n}$, $p_{ct} \coloneqq \boldsymbol{p}_c \cdot \boldsymbol{t}$ indicates the normal and tangential contact stresses with $\boldsymbol{p}_c$ the traction on Γ_c and $\boldsymbol{n}, \boldsymbol{t}$ the normal vector and right-handed tangential vector for the contact surface; δ_n and δ_t denote the magnitude of the inter-surface gap in the normal and tangential direction respectively; μ_c is the frictional coefficient; the dots in (9) denote the time derivative, hence $\dot{\delta}_t$ indicates the rate of relative slip between two body fields along the direction of $\boldsymbol{t}$. Specifically, we refer to δ_t as:

$$\dot{\delta}_{tk} = \begin{cases} v_{t2} - v_{t1}, & \text{for } k = 1, \\ v_{t1} - v_{t2}, & \text{for } k = 2. \end{cases} \tag{10}$$

where the subscript k is an index for the pair of bodies in contacts [cf. 58]; v_{tk} is the velocity component at the location of contact along the tangential direction $\boldsymbol{t}$ for different bodies.

For non-slip contact problems, the contact boundary can be viewed as a conductive boundary in terms of thermal effects, where the normal heat flux is expressed as a multiple of the surface conductance h_c and the temperature jump $[\theta]$ between two surfaces [59]:

$$q_{ck} = h_c [\theta]_k, \quad [\theta]_k = \begin{cases} \theta_2 - \theta_1, & \text{for } k = 1, \\ \theta_1 - \theta_2, & \text{for } k = 2. \end{cases} \tag{11}$$

where q_c indicates the heat flux across Γ_c. The constitutive law for the contact surface conductance h_c reads [69],

$$h_c = h_0 \left| \frac{p_{cn}}{p_0} \right|^{\epsilon} \tag{12}$$

where $p_0 > 0$ is called Vickers hardness as a regularization of the normal contact stress, h_0 is a reference conductance at $|p_{cn}| = p_0$, ϵ is a material parameter indicating the power scale with respect to p_{cn}. Notice that by picking $\epsilon = 1$, this law is further simplified into a linear relationship

$$h_c = \bar{\gamma} |p_{cn}|, \quad \bar{\gamma} \coloneqq \frac{h_0}{p_0}. \tag{13}$$

where $\bar{\gamma}$ is the stress–conductance coefficient defined as the ratio between reference conductance and the Vickers hardness, which can be regarded as a material property.

In frictional contact cases, we need to take into account the heat generated during slipping. We assume that the surface specific heat is zero and heat dissipates into both fields equally. Then the normal heat flux in (11) is modified as [73]:

$$q_{ck} = h_c [\theta]_k + \frac{1}{2} p_{ct} \dot{\delta}_t \tag{14}$$

We also assume that the frictional coefficient on the contact surface is temperature-dependent, which has the following form [57]:

$$\mu_c = \mu_{co} \frac{\langle \theta_{\text{dam}} - \max(\theta_1, \theta_2) \rangle^2}{(\theta_{\text{dam}} - \theta_{\text{ref}})^2} \tag{15}$$

where θ_{dam} indicates the temperature where the frictional response on the contact surface completely disappears; θ_{ref} is a reference temperature constant, usually chosen as the initial temperature; μ_{co} is the undamaged frictional coefficient at the reference temperature. $\langle \cdot \rangle$ are the Macaulay brackets such that $\langle x \rangle = (x + |x|)/2$

2.2.1. Specific constitutive relationships

We adopt the compressible Neo-Hookean hyperelastic model to replicate the elastic responses of the brittle materials. This hyperelasticity energy consists of two components that calculate the elastic stored energy due to volumetric and deviatoric deformation, i.e., [74]:

$$U(J) = \frac{1}{2}K(\log J)^2, \tag{16}$$

$$\overline{W}(\boldsymbol{b}_{\text{iso}}) = \frac{1}{2}G(\text{tr}(\boldsymbol{b}_{\text{iso}}) - 3). \tag{17}$$

where K and G are the bulk modulus and the shear modulus respectively. $\text{tr}(\cdot)$ is the tensor trace operation. For the thermal fields, we consider the isotropic Fourier's heat conduction law in the Eulerian form [30]:

$$\boldsymbol{q} = -\kappa \nabla_{\boldsymbol{x}} \theta, \tag{18}$$

where κ is the heat conduction coefficient. $\nabla_{\boldsymbol{x}}$ is the gradient operator on the deformed configuration.

To capture the fracture propagation with damage evolution, we adopt Rankine's damage model with linear strain-softening for brittle damage (Rankine's rotating crack model) [75]. In this theory, the damage evolution is governed by the largest effective principal tensile stress $\overline{\sigma}_m$ assuming that the damage yield function takes the form $\Phi(\overline{\sigma}_m, R) = \overline{\sigma}_m - R$ [76], where R is the damage internal variable. Φ and R should satisfy the KKT condition, which is addressed as:

$$\Phi \leq 0, \quad \dot{R} \geq 0, \quad \Phi \dot{R} = 0. \tag{19}$$

We assume that the damage is initially zero and starts evolving once $\overline{\sigma}_m$ reaches the critical stress threshold σ_f. This makes it possible to derive an explicit functional representation of the damage internal variable: $R = \max(\sigma_f, \max_t(\overline{\sigma}_m))$, where $\max_t(\cdot)$ indicates finding the largest historical value for a specific term. With this knowledge, R can be interpreted as the largest effective principal tensile stress in the stress history of a particular material point.

To complete the formulation of this damage constitutive model, the mapping function from the internal variable R to the damage scale d must be defined. This is derived from the linear strain-softening after the crack evolution is triggered [67]:

$$d(R) = \begin{cases} (1 + H_s)(1 - \frac{\sigma_f}{R}) & , \quad \sigma_f < R < \sigma_f(1 + \frac{1}{H_s}), \\ 1 & , \quad R \geq \sigma_f(1 + \frac{1}{H_s}). \end{cases} \tag{20}$$

where $H_s := \overline{H}_s l_{ch}/(1 - \overline{H}_s l_{ch})$ is the mesh-regularized damage modulus with l_{ch} indicating the mesh characteristic length [77] and $\overline{H}_s$ standing for the brittleness factor. l_{ch} is often chosen as the diagonal length of a cell in a structured grid, and $\overline{H}_s$ can be derived from the material properties with Assumption 4 in Section 2.1 (for more details, see [77]):

$$\overline{H}_s = \frac{\sigma_f^2}{2EG_f} \tag{21}$$

where E is Young's modulus and G_f is the critical energy release rate.

2.3. Governing equations for the thermo-mechanical problems

Here we briefly review the balance of mass, linear momentum, and energy for the contact problems. The balance of mass reads:

$$\rho = \rho_o / J, \tag{22}$$

where ρ and ρ_o are the mass densities on the deformed and reference volume accordingly. In the current configuration, the balance of linear momentum reads:

$$\rho \boldsymbol{a} = \nabla_{\boldsymbol{x}} \cdot \boldsymbol{\sigma} + \rho \boldsymbol{g}, \tag{23}$$

where $\boldsymbol{a}$ is the acceleration, $\boldsymbol{g}$ is the body force per mass, $\boldsymbol{\sigma} = \frac{1}{J}\boldsymbol{\tau}$ represents the Cauchy stress, $\nabla_{\boldsymbol{x}} \cdot$ indicates the divergence on the deformed configuration. An important advantage of the MPM formulation is that the grid used

to compute the residual is also doubled as the updated Lagrangian frame and hence the convection term in the acceleration in the Eulerian frame does not appear [78].

To formulate the balance of energy, we first define the internal energy per unit mass as $e := \psi + \theta\eta$. The rate of internal energy change consists of external stress power and the incoming heat flux (we ignore external heat sources). Hence, the local form of the energy balance equation reads,

$$\rho\dot{e} = \boldsymbol{\sigma} : \boldsymbol{d} - \nabla_{\boldsymbol{x}} \cdot \boldsymbol{q} \tag{24}$$

where $\boldsymbol{d} := \frac{1}{2}(\boldsymbol{l} + \boldsymbol{l}^T)$ is the symmetric part of the velocity gradient $\boldsymbol{l} = \nabla_{\boldsymbol{x}}\boldsymbol{v}$ with $\boldsymbol{v}$ representing velocity and $\boldsymbol{q}$ indicating the heat flux on the unit deformed volume. Recall that the rate of the change of internal energy is related to those of the free Helmholtz energy, temperature, and entropy, i.e.,

$$\dot{e} = \dot{\psi} + \dot{\theta}\eta + \theta\dot{\eta}, \tag{25}$$

where the time derivative of $\psi(\boldsymbol{b}, \theta, d)$ is

$$\dot{\psi} = \frac{\partial\psi}{\partial\boldsymbol{b}} : \dot{\boldsymbol{b}} + \frac{\partial\psi}{\partial\theta}\dot{\theta} + \frac{\partial\psi}{\partial d}\dot{d}, \tag{26}$$

Substituting $\eta = -\partial\psi/\partial\theta$ into (26), we have

$$\dot{\psi} + \dot{\theta}\eta = \frac{\partial\psi}{\partial\boldsymbol{b}} : \dot{\boldsymbol{b}} + \frac{\partial\psi}{\partial d}\dot{d}, \tag{27}$$

Since we only have the damage scalar as the internal variable in this formulation, we can define the internal energy dissipation following [79]:

$$\mathcal{D}_{int} = -\left(\frac{\partial\psi}{\partial d}\right)_{\boldsymbol{b},\theta}\dot{d} = \frac{1}{\rho_o}\left(\overline{\psi}^e - 3\alpha_t(\theta - \theta_0)\frac{\partial U}{\partial J}\right)\dot{d}, \tag{28}$$

where $\mathcal{D}_{int}$ refers to the internal dissipation term for the damage internal variable d.

We further implement the following equation due to $\eta = \eta(\boldsymbol{b}, \theta, d)$:

$$\theta\dot{\eta} = \theta\frac{\partial\eta}{\partial\boldsymbol{b}} : \dot{\boldsymbol{b}} + \theta\frac{\partial\eta}{\partial\theta}\dot{\theta} + \theta\frac{\partial\eta}{\partial d}\dot{d}, \tag{29}$$

Following [79], (29) is rewritten as:

$$\theta\dot{\eta} = c_F\dot{\theta} + \mathcal{H}_e + \mathcal{H}_{in}, \tag{30}$$

where

$$c_F = \theta\left(\frac{\partial\eta}{\partial\theta}\right)_{\boldsymbol{b},d}, \quad \mathcal{H}_e = \theta\left(\frac{\partial\eta}{\partial\boldsymbol{b}}\right)_{\theta,d} : \dot{\boldsymbol{b}}, \quad \mathcal{H}_{in} = \theta\left(\frac{\partial\eta}{\partial d}\right)_{\boldsymbol{b},\theta}\dot{d}, \tag{31}$$

where c_F denotes the specific heat per unit mass, $\mathcal{H}_e$ indicates the structural heating term, induced by the elastic volumetric deformation, and $\mathcal{H}_{in}$ is the structural heating term due to the damage internal variable.

To handle the partial derivatives w.r.t. η in (31), we substitute the definition of η in (6) with (1):

$$\eta = -\frac{\partial\psi}{\partial\theta} = -\frac{\partial M}{\partial\theta} - \frac{\partial\psi^t}{\partial\theta}, \tag{32}$$

Insert (32) to (31), and we have

$$c_F = -\theta\frac{\partial^2 M}{\partial\theta^2} - \theta\frac{\partial^2\psi^t}{\partial\theta^2}, \tag{33}$$

$$\mathcal{H}_e = -\theta\left[\frac{\partial^2 M}{\partial\theta\partial\boldsymbol{b}} + \frac{\partial^2\psi^t}{\partial\theta\partial\boldsymbol{b}}\right] : \dot{\boldsymbol{b}}, \tag{34}$$

$$\mathcal{H}_{in} = -\theta\left[\frac{\partial^2 M}{\partial\theta\partial d} + \frac{\partial^2\psi^t}{\partial\theta\partial d}\right]\dot{d}, \tag{35}$$

From the free energy form in Section 2.1, we observe that the coupled energy M is linear in θ, while the pure thermal energy ψ^t is independent of $\boldsymbol{b}$ and d. As such,

$$\frac{\partial^2 M}{\partial\theta^2} = 0, \qquad \frac{\partial^2\psi^t}{\partial\theta\partial\boldsymbol{b}} = \boldsymbol{0}, \qquad \frac{\partial^2\psi^t}{\partial\theta\partial d} = 0, \tag{36}$$

In addition, as M is not an explicit function of $\boldsymbol{b}$ but an explicit function of J, we can further simplify the partial derivative of M with respect to $\boldsymbol{b}$ in (34) as:

$$\frac{\partial^2 M}{\partial\theta\partial\boldsymbol{b}} : \dot{\boldsymbol{b}} = \frac{\partial^2 M}{\partial\theta\partial J}\dot{J}, \tag{37}$$

Using (36) to eliminate zero terms in (33)–(35) and insert (37) to (34), we derive the following expressions for the practical calculation of the specific heat and the structural heating terms:

$$c_F = -\theta\frac{\partial^2\psi^t}{\partial\theta^2} \quad = c, \tag{38}$$

$$\mathcal{H}_e = -\theta\frac{\partial^2 M}{\partial\theta\partial J}\dot{J} = \frac{1}{\rho_o}3\alpha_t\theta(1-d)\frac{\partial^2 U}{\partial J^2}\dot{J}, \tag{39}$$

$$\mathcal{H}_{in} = -\theta\frac{\partial^2 M}{\partial\theta\partial d}\dot{d} = -\frac{1}{\rho_o}3\alpha_t\theta\frac{\partial U}{\partial J}\dot{d}, \tag{40}$$

We finally insert all terms in (27) and (31) into (24):

$$\rho\frac{\partial\psi}{\partial\boldsymbol{b}} : \dot{\boldsymbol{b}} - \rho\mathcal{D}_{int} + \rho c_F\dot{\theta} + \rho\mathcal{H}_e + \rho\mathcal{H}_{in} = \boldsymbol{\sigma} : \boldsymbol{d} - \nabla_{\boldsymbol{x}}\cdot\boldsymbol{q} \tag{41}$$

where $\boldsymbol{\sigma} : \boldsymbol{d} = 2\rho\frac{\partial\psi}{\partial\boldsymbol{b}}\boldsymbol{b} : \boldsymbol{d} = \rho\frac{\partial\psi}{\partial\boldsymbol{b}} : \dot{\boldsymbol{b}}$ [cf. 79]. As a result:

$$\rho c_F\dot{\theta} + \rho\mathcal{H}_e + \rho\mathcal{H}_{in} = -\nabla_{\boldsymbol{x}}\cdot\boldsymbol{q} + \rho\mathcal{D}_{int}. \tag{42}$$

By rearranging Eq (42), we recover the balance of energy equation in Eq. (103) of [80]

$$\rho c_F\dot{\theta} = -\nabla_{\boldsymbol{x}}\cdot\boldsymbol{q} + \rho\mathcal{D}_{int} - \rho\mathcal{H}_e - \rho\mathcal{H}_{in}, \tag{43}$$

To complete the formulation of a thermo-mechanical boundary value problem in a deformed body Ω, we present the boundary conditions on its boundary Γ. We decompose the mechanical boundary into three parts as $\Gamma = \Gamma_u \cup \Gamma_t \cup \Gamma_c$ with $\Gamma_u \cap \Gamma_t = \Gamma_u \cap \Gamma_c = \Gamma_t \cap \Gamma_c = \varnothing$, where Γ_u is the displacement boundary, Γ_t is the traction boundary and Γ_c is the contact boundary. We decompose the thermal boundary into four parts as $\Gamma = \Gamma_\theta \cup \Gamma_q \cup \Gamma_h \cup \Gamma_c$ with $\Gamma_\theta \cap \Gamma_q = \Gamma_\theta \cap \Gamma_h = \Gamma_q \cap \Gamma_h = \varnothing$, where Γ_θ is the temperature boundary, Γ_q is the heat flux boundary, Γ_h is the conductive boundary and none of these three boundaries overlap with Γ_c. Accordingly, the boundary conditions are:

$$\begin{cases} \boldsymbol{u} = \overline{\boldsymbol{u}} & \text{on } \Gamma_u, \\ \boldsymbol{\sigma}\cdot\boldsymbol{n} = \overline{\boldsymbol{t}} & \text{on } \Gamma_t, \end{cases} \quad \begin{cases} \theta = \overline{\theta} & \text{on } \Gamma_\theta, \\ \boldsymbol{q}\cdot\boldsymbol{n} = -\overline{q} & \text{on } \Gamma_q, \\ \boldsymbol{q}\cdot\boldsymbol{n} = h(\theta_\infty - \theta) & \text{on } \Gamma_h. \end{cases} \tag{44}$$

where $\overline{\boldsymbol{u}}$ is the prescribed displacement on Γ_u; $\overline{\boldsymbol{t}}$ is the applied traction on Γ_t; $\overline{\theta}$ is the prescribed temperature on Γ_θ; $\overline{q}$ is the applied normal heat flux on Γ_q; h is the surface conductive coefficient and θ_∞ is the ambient temperature on Γ_h. On Γ_c, we enforce the mechanical contact governing equations (8) and (9) and the contact heat conduction equation (14) instead of prescribed boundary conditions.

3. Numerical implementation with MPM

In this section, we describe the numerical implementation of the mathematical framework that captures the interplay between evolving contacts and dynamic fracture under non-isothermal conditions. We first briefly review the algorithm of the MPM that updates the updated Lagrangian frame with material points and the implication of this treatment to handle the convection of heat in the finite deformation range. Then, we elaborate on the algorithms that detect contact and calculate separation displacement among brittle bodies for dynamic thermo-mechanics problems. We then discuss the contact calculation with a focus on the thermal effect. The implementation algorithm is concluded at the end.

3.1. An overview of MPM

In this MPM formulation, all physical variables (such as $\boldsymbol{b}$, θ, and d) are stored at particles as the Lagrangian description. These particles are connected with a grid using weighting functions whose augments are the relative positions between particles and the grid. We then calculate the unbalanced variables (such as acceleration for the balance of momentum) of nodes and project the information back to particles. After one MPM time step, the deformed grid is reset to the initial configuration as structured since it only works to connect particles. Therefore, the framework of MPM belongs to the updated Lagrangian form without any special treatment. For the sake of clarity, $\boldsymbol{x}$ refers to the current location; the subscript i indicates variables attribute at the discrete grid node i, and the subscript p is used to present variables at particles.

The weak form of the balance of momentum in the current configuration is:

$$\int_{\Omega} \boldsymbol{w} \cdot \rho \boldsymbol{a} d\Omega = -\int_{\Omega} \nabla_{\boldsymbol{x}} \boldsymbol{w} : \boldsymbol{\sigma} d\Omega + \int_{\Omega} \boldsymbol{w} \cdot \rho \boldsymbol{b} d\Omega + \int_{\Gamma_t} \boldsymbol{w} \cdot \bar{t} d\Gamma + \int_{\Gamma_c} \boldsymbol{w} \cdot \boldsymbol{p}_c d\Gamma, \tag{45}$$

where $\boldsymbol{w}$ is the admissible test function. The discrete form of the momentum equation is [81,82]:

$$m_i \boldsymbol{a}_i = \boldsymbol{f}_i^{\text{ext}} - \boldsymbol{f}_i^{\text{int}} + \boldsymbol{f}_i^{\text{cont}}, \tag{46}$$

where m_i, $\boldsymbol{a}_i$, $\boldsymbol{f}_i^{\text{ext}}$, $\boldsymbol{f}_i^{\text{int}}$, and $\boldsymbol{f}_i^{\text{cont}}$ represent the mass, acceleration, external force, internal force and the contact force at grid node i, respectively. These nodal attributes are calculated with the following equations:

$$m_i = \sum_p m_p \overline{S}_{ip}, \tag{47}$$

$$\boldsymbol{f}_i^{\text{ext}} = \sum_p m_p \overline{S}_{ip} \boldsymbol{g}_p + \int_{\Gamma_t} S_i \bar{\boldsymbol{t}} \, d\Gamma, \tag{48}$$

$$\boldsymbol{f}_i^{\text{int}} = \sum_p V_p \boldsymbol{\sigma}_p \cdot \overline{\nabla_{\boldsymbol{x}} S_{ip}}, \tag{49}$$

$$\boldsymbol{f}_i^{\text{cont}} = \int_{\Gamma_c} S_i \boldsymbol{p}_c \, d\Gamma. \tag{50}$$

where m_p, V_p, $\boldsymbol{g}_p$, $\boldsymbol{\sigma}_p$ represents the mass, deformed volume, body force, and the Cauchy stress at particle p, respectively, the operator $\sum_p$ indicates summing the influence of the neighbor particles at a node [26], S_i indicates the standard grid node basis function, $\overline{S}_{ip}$ and $\overline{\nabla_{\boldsymbol{x}} S}_{ip}$ are the weighting function and its gradient for the mapping between node i and particle p.

Noting that $\overline{S}_{ip}$ links the particles and the grid, we here adopt the Convected Particle Domain Interpolation (CPDI) to compute $\overline{S}_{ip}$ for accuracy, as proposed in [83]. Assuming that the particle domain is a parallelogram and that the deformation gradient is approximately constant over the particle domain, the particle domain deforms according to

$$\begin{cases} \boldsymbol{r}_1 = \boldsymbol{F} \cdot \boldsymbol{r}_1^0, \\ \boldsymbol{r}_2 = \boldsymbol{F} \cdot \boldsymbol{r}_2^0, \end{cases} \tag{51}$$

where $(\boldsymbol{r}_1^0, \boldsymbol{r}_2^0)$ and $(\boldsymbol{r}_1, \boldsymbol{r}_2)$ are the vectors defining a particle domain at the initial and updated configuration, respectively. For the standard FE 4-node (Q4) element, which is adopted in this work, the weighting function and its gradient are

$$\overline{S}_{ip} \cong \frac{1}{4}\left[S_i(\boldsymbol{x}_1^p) + S_i(\boldsymbol{x}_2^p) + S_i(\boldsymbol{x}_3^p) + S_i(\boldsymbol{x}_4^p)\right], \tag{52}$$

$$\overline{\nabla_{\boldsymbol{x}} S}_{ip} \cong \frac{1}{2V_p}\left\{(S_i(\boldsymbol{x}_1^p) - S_i(\boldsymbol{x}_3^p))\begin{bmatrix} r_{1y}^n - r_{2y}^n \\ r_{2x}^n - r_{1x}^n \end{bmatrix} + (S_i(\boldsymbol{x}_2^p) - S_i(\boldsymbol{x}_4^p))\begin{bmatrix} r_{1y}^n + r_{2y}^n \\ -r_{1x}^n - r_{2x}^n \end{bmatrix}\right\}, \tag{53}$$

where $\boldsymbol{x}_\alpha^p$ $\alpha = 1, 2, 3, 4$ are the positions of the corners of the parallelogram, (r_{1x}, r_{1y}) and (r_{2x}, r_{2y}) are the components of vectors of $\boldsymbol{r}_1^n$ and $\boldsymbol{r}_2^n$, respectively, and the superscript n denotes the nth time step.

We now consider the discrete energy equation. Starting from the variation of the energy equation in terms of temperature with an arbitrary scalar testing function w:

$$\int_{\Omega} w\rho c\dot{\theta} d\Omega = \int_{\Omega} \nabla_{\boldsymbol{x}} w \cdot \boldsymbol{q} d\Omega - \int_{\Omega} w\mathcal{H}_e d\Omega + \int_{\Omega} w(\mathcal{D}_{int} - \mathcal{H}_{in}) d\Omega + \int_{\Gamma_q} w\bar{q} d\Gamma + \int_{\Gamma_h} wh(\theta_{\infty} - \theta) d\Gamma + \int_{\Gamma_c} wq_{cn}\, d\Gamma, \tag{54}$$

Following similar logics in the derivation of (46), the form of discrete energy equation is:

$$C_i\dot{\theta}_i = Q_i^{\text{ext}} + Q_i^{\text{int}} + Q_i^{\text{ecpl}} + Q_i^{\text{dcpl}} + Q_i^{\text{cont}}, \tag{55}$$

where C_i and $\dot{\theta}_i$ indicate the heat capacity and temperature evolution rate for at grid node i; Q_i^{ext}, Q_i^{int}, Q_i^{ecpl}, Q_i^{dcpl}, Q_i^{cont} represent the external, internal, elastic-coupling, damage-coupling, and contact thermal loads at grid node i, respectively. These nodal attributes are calculated with the following equations:

$$C_i = \sum_p m_p c_p \overline{S}_{ip}, \tag{56}$$

$$Q_i^{\text{ext}} = \int_{\Gamma_q} S_i \bar{q}\, d\Gamma + \int_{\Gamma_q} S_i h(\theta_{\infty} - \theta)\, d\Gamma, \tag{57}$$

$$Q_i^{\text{int}} = \sum_p V_p \boldsymbol{q}_p \cdot \overline{\nabla_{\boldsymbol{x}} S}_{ip}, \tag{58}$$

$$Q_i^{\text{ecpl}} = -\sum_p V_p \overline{S}_{ip} (\mathcal{H}_e)_p, \tag{59}$$

$$Q_i^{\text{dcpl}} = \sum_p V_p \overline{S}_{ip} \left((\mathcal{D}_{int})_p - (\mathcal{H}_{in})_p \right), \tag{60}$$

$$Q_i^{\text{cont}} = \int_{\Gamma_c} S_i q_{cn}\, d\Gamma. \tag{61}$$

where c_p, θ_p, $\boldsymbol{q}_p$ indicate the specific heat, the temperature, and the heat flux at each particle p, respectively; $(\mathcal{D}_{int})_p$, $(\mathcal{H}_e)_p$, and $(\mathcal{H}_{in})_p$ are the internal dissipation, the elastic structural heating and internal variable induced heating terms at each particle p.

At the end of one MPM time step, we will perform time integration on all nodal unbalanced variables and update the material fields at particles accordingly. There are two popular time integration strategies to solve a fully coupled system, i.e. the monolithic integration scheme and the staggered integration scheme. The monolithic time integration requires the equations for different fields to be solved simultaneously [84]. For this approach, an iterative strategy is usually required to determine the amount of increment in both thermal and mechanical fields since the equations are strongly coupled together, which increases its computational cost significantly. In the staggered time integration, however, the entire system is split into individual fields that perform time marching separately [85]. With the explicit Euler time integration scheme, this approach evolves individual fields sequentially based on the latest information from the thermal and mechanical fields [86]. As a result, the staggered scheme is much more efficient than the monolithic scheme. In this paper, we adopt the staggered time-stepping scheme for the time integration in MPM.

We update thermal fields using:

$$\theta_p^{n+1} = \theta_p^n + \Delta t \sum_i \dot{\theta}_i^{n+1} \overline{S}_{ip}, \tag{62}$$

$$\boldsymbol{q}_p^{n+1} = \boldsymbol{q}_p^n + \kappa_p \Delta t \sum_i \dot{\theta}_i^{n+1} \overline{\nabla_{\boldsymbol{x}} S}_{ip}, \tag{63}$$

where κ_p is the heat conductance at each particle p; Δt is the time increment; all superscripts $n, n+1$ refer to the variable at the nth, $n+1$th time step.

When updating velocities, we use a combination of fluid-implicit-particle (FLIP) and particle-in-cell (PIC) velocity update scheme [87]:

$$\boldsymbol{v}_p^{n+1} = (1-\zeta) \left(\boldsymbol{v}_p^n + \Delta t \sum_i \boldsymbol{a}_i^{n+1} \overline{S}_{ip} \right) + \zeta \sum_i \boldsymbol{v}_i^{n+1} \overline{S}_{ip} \tag{64}$$

where $\boldsymbol{v}_i$, $\boldsymbol{v}_p$ are velocities at grid node i or particle p, respectively. ζ is a coefficient indicating the portion of PIC update in the velocity evolution scheme. $\zeta = 1$ gives a pure PIC update of velocities, while $\zeta = 0$ gives a pure FLIP velocity update. Note that, because the PIC velocity update scheme can be regarded as a spatial smoothing scheme on the velocity field, it may damp out the high-frequency oscillations [82]. The locations and deformation gradients associated with the pth material points are updated as follows:

$$\boldsymbol{x}_p^{n+1} = \boldsymbol{x}_p^n + \Delta t \sum_i \boldsymbol{v}_i^{n+1} \overline{S}_{ip}, \tag{65}$$

$$\boldsymbol{F}_p^{n+1} = \left(\boldsymbol{I} + \Delta t \sum_i \boldsymbol{v}_i^{n+1} \otimes \overline{\nabla_{\boldsymbol{x}} S_{ip}} \right) \boldsymbol{F}_p^n. \tag{66}$$

where $\boldsymbol{x}_p$ and $\boldsymbol{F}_p$ are the location of particle center and the deformation gradient at p, respectively; $\boldsymbol{I}$ denotes the 2nd-order identity tensor; $\otimes$ is the dyadic product operator. The stress tensor and damage scalar are updated upon obtaining the updated mechanical and thermal fields.

3.2. The damage field-gradient material partitioning

To identify the locations of the contacts, we employ the partition criterion first proposed in [26] where we would use the gradient of damage field at the nodes of grid i as an indicator function to partition the continuum bodies and identify the potential contacted interfaces. In essence, this approach detects contacts by assuming that contacts may take place at damaged interfaces, and one may detect contacts by identifying traits of the gradient of damage field projected onto the background mesh to identify the set of contact nodes and compute the relative separation between the contacted bodies. While previous works such as [25] and [88] may require one to assigning labels or level set to a subset of material points to identify the bodies in contacts, the treatment in [26] bypasses this requirement and hence is ideal for simulating fragmentation where self-contacts must be detected [89]. With ith sub-domain of bodies partitioned via the node set i, we can elaborate on the relative velocity between different parts of the body to further determine the contact interactions. The partitioning scheme is briefly reviewed here for completeness.

The normalized smoothed damage field is constructed as:

$$\overline{D}(\boldsymbol{x}) = \frac{D(\boldsymbol{x})}{\mathcal{S}(\boldsymbol{x})}, \text{ with } D(\boldsymbol{x}) := \sum_p \max(s_p, d_p)\omega(\bar{r}), \quad \mathcal{S}(\boldsymbol{x}) := \sum_p \omega(\bar{r}), \tag{67}$$

where s_p is a boundary particle indicator such that $s_p = 1$ for boundary particles and $s_p = 0$ otherwise, d_p is the damage parameter at particle p, $\omega(\bar{r}) = 1 - 3\bar{r}^2 + 2\bar{r}^3$ for $0 \le \bar{r} \le 1$ and $\omega(\bar{r}) = 0$ elsewhere; $\bar{r} = \|\boldsymbol{x} - \boldsymbol{x}_p\|/r_p$ is a normalized distance measure with a support radius of r_p. For plane 2D problems, r_p is usually chosen as the diagonal length of the background cells. The setting of s_p is adopted to consider the self-contact (different bodies existing initially), and the setting of $\mathcal{S}(\boldsymbol{x})$ is employed to eliminate the boundary effect.

The gradient of damage $\nabla_{\boldsymbol{x}} \overline{D}(\boldsymbol{x})$ could help identify particles from different fields. Suppose there is a developing crack crossing a grid node, which makes field partitioning necessary at that node. Usually, the degree of damage of a particle closer to the surface is much larger than that of internal particles, so the damage gradients typically point from surfaces (material boundary) to internal regions. Therefore, particles belonging to different material fields in the influencing region of a grid node generally have damage gradients pointing in relatively opposite directions. To describe this mathematically, we claim the following criterion for field partition at grid nodes:

$$\exists \text{ particles } p_1, p_2 \text{ in the vicinity of node } i \text{ s.t.} \quad \nabla_{\boldsymbol{x}} \overline{D}_i \cdot \nabla_{\boldsymbol{x}} \overline{D}_{p_1} > 0 \text{ and } \nabla_{\boldsymbol{x}} \overline{D}_i \cdot \nabla_{\boldsymbol{x}} \overline{D}_{p_2} < 0. \tag{68}$$

where $\nabla_{\boldsymbol{x}} \overline{D}_i$ refers to the gradient of $\overline{D}$ at i, and $\nabla_{\boldsymbol{x}} \overline{D}_p = \nabla_{\boldsymbol{x}} \overline{D}(\boldsymbol{x}_p)$. For (68) to be valid, it is necessary that $\nabla_{\boldsymbol{x}} \overline{D}_i \neq \boldsymbol{0}$, but around a fully damaged region, we probably get the value close to zero. Therefore, a nonlocal approach is required to determine the grid-node damage gradient. Since we only compare the sign of vector dot products rather than the magnitude and the order of numbering for material fields does not matter, the following rule for determining the nonlocal damage gradient is adopted:

$$\nabla_{\boldsymbol{x}} \overline{D}_i = \nabla_{\boldsymbol{x}} \overline{D}(\boldsymbol{x}_i^{max}) \text{ where } \boldsymbol{x}_i^{max} = \arg \max_{|\boldsymbol{x} - \boldsymbol{x}_i| < r_g} |\nabla_{\boldsymbol{x}} \overline{D}(\boldsymbol{x})|. \tag{69}$$

where $\boldsymbol{x}_i$ is the position of grid node i, r_g is a support radius for the range of nonlocal searching, usually chosen as the diagonal length of the grid cell, and $|\cdot|$ stands for the vector norm operation. To avoid maximizing a complicated function in a continuous space, we calculate (69) by searching for the damage gradient with the maximum vector norm over $\nabla_{\boldsymbol{x}}\overline{D}_p$ located at particle centers. Once we divide the bodies into different fields, the update scheme should be performed separately for different bodies.

Since we use an evolving damage field to identify the location of the fractured interface, an important issue is that there could be incompletely damaged region(s) that should not be regarded as actually fractured zones during the fracture. To resolve this issue, we may determine the degree of damage at a grid node. If a grid node is completely damaged (fractured), the two different material fields may separate apart and we should apply the contact algorithm. Otherwise, cohesion should be allowed between different fields, making the partitioned material fields still evolve as a single entity. To define a separable condition that distinguishes the separable and non-separable state at a grid node, we adopt the average nodal damage for two material fields to evaluate the state of damage [26]:

$$\overline{D}_{ki} = \frac{\sum_{kp} m_p d_p \overline{S}_{ip}}{m_{ki}}, \tag{70}$$

where the subscript k denotes the k-body. The separable condition is: a grid node is separable if its maximum and minimum averaged nodal damages reach some critical values, namely:

$$\max(\overline{D}_{1i}, \overline{D}_{2i}) > \overline{D}^{\text{cr}}, \quad \min(\overline{D}_{1i}, \overline{D}_{2i}) > \overline{D}^{\text{min}}, \tag{71}$$

where $\overline{D}^{\text{cr}}$ indicates the critical averaged nodal damage required for separation for the maximum over $\overline{D}_{1i}$ and $\overline{D}_{2i}$ to reach, and $\overline{D}^{\text{min}}$ indicates the minimum averaged nodal damage required for separation for the minimum over $\overline{D}_{1i}$ and $\overline{D}_{2i}$ to reach.

If the partitioned fields are separable from each other, we will further apply a thermo-contact algorithm to determine all the contact interactions, especially the contact forces and contact thermal loads. For cases where the partitioned fields are not separable, both fields evolve as a single one integrally.

3.3. Calculations of the contact force and heat flux across contacts

In the MPM, a momentum correction scheme is widely used to approximate the contact forces at grid nodes [90]. We are specifically interested in a double-field formulation of material partitioning for contact modeling. To formulate the momentum conservation over both fields, we define the center-of-mass velocity as an evaluation of the averaged velocity if merging both fields into one: [90,91]:

$$\boldsymbol{v}_i^{\text{cm}} = \frac{\sum_k^2 m_{ki} \hat{\boldsymbol{v}}_{ki}}{\sum_k^2 m_{ki}}, \tag{72}$$

where $\boldsymbol{v}_i^{\text{cm}}$ is the nodal center-of-mass velocity, $\hat{\boldsymbol{v}}_{ki}$ represents the updated nodal velocity for the kth material field before contact adjustment.

A potential in-contact node is defined as a grid node with particles from different material fields in its vicinity. However, real contact interactions only take place when two material fields have a trend of inter-penetration. We need the following criterion to distinguish if two material fields are coming into contact:

$$(\hat{\boldsymbol{v}}_{ki} - \boldsymbol{v}_i^{\text{cm}}) \cdot \boldsymbol{n}_{ki} > 0, \tag{73}$$

where $\boldsymbol{n}_{ki}$ is the outward surface normal vector based on the nodal mass gradient [26,82]:

$$\boldsymbol{n}_{1i} \coloneqq \frac{1}{|\hat{\boldsymbol{n}}_{1i} - \hat{\boldsymbol{n}}_{2i}|}(\hat{\boldsymbol{n}}_{1i} - \hat{\boldsymbol{n}}_{2i}), \quad \boldsymbol{n}_{2i} \coloneqq -\boldsymbol{n}_{1i} \text{ with } \hat{\boldsymbol{n}}_{ki} = \frac{\sum_{kp} m_p \overline{\nabla_{\boldsymbol{x}} S}_{ip}}{|\sum_{kp} m_p \overline{\nabla_{\boldsymbol{x}} S}_{ip}|}. \tag{74}$$

Once contact is confirmed at a grid node, we will perform the calculation of contact forces. The determination of normal contact forces should address the normal KKT conditions by eliminating potential inter-penetration. Subject to momentum conservation, the normal contact force f_{ni}^{cont} at node i is calculated as:

$$f_{ni}^{\text{cont}} = \frac{1}{\Delta t} m_{ki}(\boldsymbol{v}_i^{\text{cm}} - \hat{\boldsymbol{v}}_{ki}) \cdot \boldsymbol{n}_{ki}, \tag{75}$$

One can verify that substituting k with either 1 or 2 into (75) gives the same result. Following the same logic of momentum correction, the tangential contact forces should be calculated as: $f_{ti}^{\text{cont}} = \frac{1}{\Delta t} m_{ki}(\boldsymbol{v}_i^{cm} - \hat{\boldsymbol{v}}_{ki}) \cdot \boldsymbol{t}_{ki}$, where $\boldsymbol{t}_{ki}$ is the right-handed contact tangential vector perpendicular to $\boldsymbol{n}_{ki}$. However, the tangential KKT conditions specify that the tangential contact forces cannot exceed $\mu_c |f_{ni}^{\text{cont}}|$. This requires the following correction on the tangential contact forces:

$$f_{ti}^{\text{cont}} = \min\{|\hat{f}_{ti}^{\text{cont}}|\,,\ \mu_c |f_{ni}^{\text{cont}}|\} \cdot \text{sign}(\hat{f}_{ti}^{\text{cont}}), \quad \hat{f}_{ti}^{\text{cont}} := \frac{1}{\Delta t} m_{ki}(\boldsymbol{v}_i^{cm} - \hat{\boldsymbol{v}}_{ki}) \cdot \boldsymbol{t}_{ki}, \tag{76}$$

Combining the normal and tangential components gives an expression for total the nodal contact forces:

$$\boldsymbol{f}_{ki}^{\text{cont}} = f_{ni}^{\text{cont}} \cdot \boldsymbol{n}_{ki} + f_{ti}^{\text{cont}} \cdot \boldsymbol{t}_{ki}. \tag{77}$$

We now focus on deriving an expression for the contact thermal load term Q_{ki}^{cont}. For the simplicity of derivation, we assume that the power scale $\epsilon = 1$ so that the simplified contact heatflux constitutive law (13) is used, and $\bar{\gamma}$ is uniform all over the contact boundary. We start by inserting (13) and (14) into (61):

$$Q_{ki}^{\text{cont}} = \int_{\Gamma_c} \left[\bar{\gamma}\, p_{cn} [\theta]_k - \frac{1}{2} p_{ct} \dot{\delta}_t \right] S_i \, d\Gamma, \tag{78}$$

Extracting the temperature jump $[\theta]$ and the relative slip rate $\dot{\delta}_t$ out of the integral in (78), we have:

$$Q_{ki}^{\text{cont}} = \bar{\gamma} [\theta]_{ki}^{\text{avg}} \int_{\Gamma_c} p_{cn} S_i \, d\Gamma - \frac{1}{2} (\dot{\delta}_t)_{ki}^{\text{avg}} \int_{\Gamma_c} p_{ct} S_i \, d\Gamma, \tag{79}$$

where $[\theta]_{ki}^{\text{avg}}$ and $(\dot{\delta}_t)_{ki}^{\text{avg}}$ are the averaged temperature jump and slip rate observed at the kth material field at node i, w.r.t. the original integral in (78). For $[\theta]_{ki}^{\text{avg}}$, we can use the assembled nodal temperatures as a practical approximation:

$$[\theta]_{ki}^{\text{avg}} \approx \begin{cases} \theta_{2i} - \theta_{1i} := [\theta]_{1i} & k = 1, \\ \theta_{1i} - \theta_{2i} := [\theta]_{2i} & k = 2. \end{cases} \tag{80}$$

For contacts with smooth surfaces, we assume that the spatial variation of contact surface normal vector is sufficiently low such that the following approximation for normal and tangential contact forces holds:

$$f_{ni}^{\text{cont}} \approx \int_{\Gamma_c} p_{cn} S_i \, d\Gamma, \quad f_{ti}^{\text{cont}} \approx \int_{\Gamma_c} p_{ct} S_i \, d\Gamma. \tag{81}$$

Substituting (80) and (81) into (79) gives an expression for calculating the nodal thermal contact load term:

$$Q_{ki}^{\text{cont}} \approx \bar{\gamma} [\theta]_{ki} \cdot f_{ni}^{\text{cont}} - \frac{1}{2} (\dot{\delta}_t)_{ki}^{\text{avg}} \cdot f_{ti}^{\text{cont}}. \tag{82}$$

Remark 1 (*Alternative Formulation for the Computation of the Contact Force*)**.** The focus of this work is to simulate dynamic multi-body contact under a high loading rate in which case the contact model is primarily designed for capturing the conservation of momentum during collision. To improve efficiency, the prevention of interpenetration of the contacts in the dynamic MPM simulations is often enforced via a collision contact algorithm that balances the momentum of the collided bodies, rather than directly enforcing the interpenetration constraints, as we explained in this section [cf. 26,90,92].

For quasi-static contact mechanics problem, the collision MPM contact algorithm that updates the velocity field may not be suitable and hence an alternative formulation that accurately resolves the static contact forces based on gap function is presented here for completeness. This alternative formulation is used in the Hertzian contact numerical example (see Section 4.1). To resolve the contact precisely for the quasi-static case where the velocity is negligible, one may calculate the gap function between the two interfaces and obtain the force required to prevent the interpenetration. An implicit MPM model dedicated to quasi-static contact problems can be found in our previous work that generates the gap function via a level set approach, i.e., [93]. A comprehensive review on this subject can be found in [69].

For the ease of implementation, we employ a penalty method to relate normal contact pressures from gap function values:

$$p_{cn} = \kappa_n \delta_n \tag{83}$$

where κ_n is a normal penalty parameter for interpenetration and δ_n is the normal component of the gap function. In the tangential direction, the Coulomb friction law can be implemented in a manner similar to an elasto-plastic material model. To describe this behavior, we decompose the tangential slip into an "elastic" and a non-recoverable "plastic" part: $\delta_t = \delta_t^e + \delta_t^p$ [94]. The constitutive law for the tangential frictional response is then stated as follows:

$$\begin{aligned} &\phi(p_{ct}, p_{cn}) := |p_{ct}| - \mu_c |p_{cn}| \ \leq \ 0, \\ &\dot{\delta}_t^p = \dot{\lambda} \frac{p_{ct}}{|p_{ct}|}, \quad \dot{\lambda} \geq 0, \quad \dot{\lambda}\phi = 0. \end{aligned} \tag{84}$$

where ϕ is termed the slip function (analogous to yield function in theories of plasticity) [25], and $\dot{\lambda}$ indicates the slip rate. The tangential contact traction is then calculated as:

$$p_{ct} = \kappa_t(\delta_t - \delta_t^p) \tag{85}$$

where κ_t is the tangential penalty parameter. For frictional contacts, the traction on the contact boundary is $\boldsymbol{p}_c = p_{cn}\boldsymbol{n} + p_{ct}\boldsymbol{t}$. Insert this expression for $\boldsymbol{p}_c$ into (50):

$$\boldsymbol{f}_i^{\text{cont}} = \int_{\Gamma_c} S_i \left(\kappa_n \delta_n \cdot \boldsymbol{n} + \kappa_t(\delta_t - \delta_t^p) \cdot \boldsymbol{t}\right) d\Gamma \tag{86}$$

For the practical calculation of $\boldsymbol{f}_i^{\text{cont}}$ in (86), we adopt the concept of boundary layer following [95], where we re-express (86) with the following manner:

$$\boldsymbol{f}_i^{\text{cont}} \approx \sum_p s_p \left[\frac{1}{l_p} S_{ip} \left(\kappa_n \delta_{np} \cdot \boldsymbol{n}_p + \kappa_t(\delta_{tp} - \delta_{tp}^p) \cdot \boldsymbol{t}_p\right)\right] \tag{87}$$

where $\delta_{np}, \delta_{tp}, \delta_{tp}^p$ are the normal gap, the total tangential gap, and the plastic part of the tangential gap at particle p, respectively. $\boldsymbol{n}_p$ and $\boldsymbol{t}_p$ indicate the normal and tangential directions at particle p. l_p is the thickness of particle p in the contact normal direction. The expression inside the summation is multiplied by the boundary indicator s_p such that only the values at boundary particles are used to determine the integrated nodal contact force.

3.4. Algorithms for MPM with evolving thermo-mechanical contacts

In this section, we elaborate on the time-stepping algorithm and provide an algorithmic overview for the implementation with MPM. In each time step, we first construct a particle-to-grid projection and obtain the smoothed damage-gradient field. Next, we introduce a thermal–mechanical sub-stepping algorithm where an isothermal split enables us to solve the thermo-mechanical problems by updating the temperature and displacement field sequentially [66,96–99]. The sequential solver first updated the temperature (and heat flux) field by solving the balance of energy with a fixed displacement field. Following the updates of the thermal fields, the mechanical fields (displacement and damage) are updated by solving the balance of linear momentum equation. Like other operator-splitting schemes, this sequential approach may lead to consistency issues as such the time step must be sufficiently small to avoid departure from the equilibrium states. However, since the upper bound for the stable time step for the explicit time integrator is usually small, this issue is usually not significant [81].

Algorithm 1 Sequential solver for thermo-mechanical problems with evolving contacts

1: Calculate the weight functions $\overline{S}_{ip}$ and the corresponding gradients $\overline{\nabla_{\boldsymbol{x}} S_{ip}}$ between material points and grid nodes.
2: Calculate the smoothed damage field $\overline{D}_p$ and the corresponding gradient $\nabla_{\boldsymbol{x}} \overline{D}_p$ for all particles.
3: Find the damage gradient $\nabla_{\boldsymbol{x}} \overline{D}_i$ for all nodes.
4: For each node, determine if it is cracking or undergoing contact with (68).
5: Evolve the thermal fields for all particles. See Algorithm 2.
6: Evolve the kinematic and mechanical fields for all particles. See Algorithm 3.

The overall explicit algorithm is listed in Algorithm 1. The detailed time integration algorithms for individual thermal or mechanical fields are provided in Algorithms 2 and 3 respectively.

Algorithm 2 Incremental updates for the MPM thermal fields

Calculate the nodal temperature evolution rate:
for all node i **do**
  if Eq. (68) holds true **then**
    Calculate C_{ki} for the kth material field via (56).
    Calculate Q_{ki}^{ext}, Q_{ki}^{int}, Q_{ki}^{ecpl}, Q_{ki}^{dcpl} for the kth material field via (57)–(60).
    Find the total nodal thermal load without contact adjustment: $\hat{Q}_{ki} = Q_{ki}^{\text{ext}} + Q_{ki}^{\text{int}} + Q_{ki}^{\text{ecpl}} + Q_{ki}^{\text{dcpl}}$.
    if (71) holds true **then**
      Calculate Q_{ki}^{cont} from (82) using the mechanical results from the last time step.
    else
      Obtain Q_{ki}^{cont} such that $\dot{\theta}_{1i} = \dot{\theta}_{2i} = \frac{\hat{Q}_{1i}+\hat{Q}_{2i}}{C_{1i}+C_{2i}}$ after adjustment on the contact thermal loads.
    Adjust the rate of temperature change: $\dot{\theta}_{ki} = \frac{\hat{Q}_{ki}+Q_{ki}^{\text{cont}}}{C_{ki}}$.
  else
    Calculate single-field C_i, Q_{ki}^{ext}, Q_{ki}^{int}, Q_{ki}^{ecpl}, Q_{ki}^{dcpl} via (56) ~ (60) (where $k = 1$ only)
    Calculate the single-field $\dot{\theta}_{ki}$ ($k = 1$) with (55).
Update all particle temperatures via (62).
Update the nodal temperature field using the updated particle temperatures:
for all node i **do**
  if (68) holds true **then**
    Calculate the nodal temperature at different fields: $\theta_{ki}^{n+1} = \frac{1}{C_{ki}} \sum_{kp} m_p c_p \theta_p^{n+1} \overline{S}_{ip}$
  else
    Update the single-field nodal temperature: $\theta_i^{n+1} = \frac{1}{C_i} \sum_p m_p c_p \theta_p^{n+1} \overline{S}_{ip}$
Update all particle heat fluxes with (63).

4. Numerical examples

This section presents several numerical examples to verify and validate the implementation of the MPM contact models and demonstrate the capacity of the proposed model in handling evolving multi-body thermo-mechanical contacts due to fracture and damage. We first verify the implementation of the MPM contact models with a Hertzian contact problem and a thermal contact problem. Simulation results of these two examples are compared with analytical solutions and in the first example, a mesh refinement study has been conducted. Furthermore, a validation exercise against the Kalthoff–Winkler dynamic fracture experiment is included to test whether the Rankine damage model implemented in the MPM framework may replicate the same crack pattern observed in experiments. We then demonstrate the capacity of the model to simulate thermal–mechanical damage and contact mechanics for multiple bodies in contact. A disk-squish problem is introduced to demonstrate the MPM model's capacity to solve multi-body thermo-mechanical contact problems, while a three-grain particle fragmentation problem is used to demonstrate the capability to simulate evolving thermo-mechanical contacts during the fracture and subsequent fragmentation process. We then analyze how impact velocity affects the damage, fracture, and fragmentation of particle assemblies during the non-isothermal fragmentation process.

4.1. Verification against Hertz's contact benchmark problem

This numerical example is included to verify the implementation of the MPM simulations by comparing the analytical solution for a Hertz contact problem with non-flat contact surfaces. We replicate the same simulation configuration previously used in [25] while the height of the body is changed to 4 mm, as shown in Fig. 1. Body 1 exhibits a 10 GPa Young's modulus of 10 GPa and 0 Poisson ratio, while Body 2 is considered rigid. The corresponding analytical solutions for the radius of the contact area b and the maximum contact pressure $p_{\max}$ are listed in Eq. (88) [cf. 14,100,101],

$$b = 2\sqrt{\frac{2FR}{\pi E'}}, \qquad p_{\max} = \frac{2F}{\pi b} \tag{88}$$

Algorithm 3 Incremental updates for the MPM mechanical fields

Calculate the nodal acceleration:
for all node i **do**
  if (68) holds true **then**
    Calculate m_{ki} with (47) and $\overline{D}_{ki}$ via (70) for the kth material field.
    Calculate the nodal velocities for both material fields with: $m_{ki}\boldsymbol{v}_{ki}^{n} = \sum_{kp} m_p \boldsymbol{v}_p^n \overline{S}_{ip}$.
    Find the contact normal vectors $\boldsymbol{n}_{ki}$ via (74).
    Calculate $\boldsymbol{f}_{ki}^{\text{ext}}$ and $\boldsymbol{f}_{ki}^{\text{int}}$ via (48) and (49).
    Update $\hat{\boldsymbol{v}}_{ki}$ without contact adjustment: $\hat{\boldsymbol{v}}_{ki}^{n+1} = \boldsymbol{v}_{ki}^{n} + \Delta t \frac{\boldsymbol{f}_{ki}^{\text{ext}} - \boldsymbol{f}_{ki}^{\text{int}}}{m_{ki}}$
    if (71) holds true **then**
      Calculate the center-of-mass velocity $\boldsymbol{v}_i^{\text{cm}}$ from (72).
      if $\boldsymbol{n}_{1i} \cdot (\hat{\boldsymbol{v}}_{1i}^{n+1} - \boldsymbol{v}_i^{\text{cm}}) > 0$ **then**
        Find the frictional coefficient with (15) using the updated temperatures θ_{1i}, θ_{2i}.
        Calculate the contact force $\boldsymbol{f}_{ki}^{\text{cont}}$ via (77).
      else
        Set $\boldsymbol{f}_{ki}^{\text{cont}}$ as zero vectors.
    else
      Obtain $\boldsymbol{f}_{ki}^{\text{cont}}$ such that $\boldsymbol{v}_{1i}^{n+1} = \boldsymbol{v}_{2i}^{n+1} = \boldsymbol{v}_i^{\text{cm}}$ after contact adjustment on nodal velocities.
    Adjust the nodal velocities with: $\boldsymbol{v}_{ki}^{n+1} = \hat{\boldsymbol{v}}_{ki}^{n+1} + \frac{\boldsymbol{f}_{ki}^{\text{cont}}}{m_{ki}} \Delta t$
    Find the nodal accelerations for both fields with (46).
  else
    Calculate the single-field nodal attributes m_{ki}, $\boldsymbol{f}_{ki}^{\text{ext}}$, $\boldsymbol{f}_{ki}^{\text{int}}$ (where $k = 1$ only).
    Calculate the single-field nodal velocities with: $m_{ki}\boldsymbol{v}_{ki}^{n} = \sum_p m_p \boldsymbol{v}_p^n \overline{S}_{ip}$ (where $k = 1$ only).
    Calculate the nodal acceleration (46) (where $k = 1$ only).
    Update the nodal velocity with: $\boldsymbol{v}_{ki}^{n+1} = \boldsymbol{v}_{ki}^{n} + \Delta t \cdot \boldsymbol{a}_{ki}^{t}$ (where $k = 1$ only).
Update the particle locations, velocities, and deformation gradients via (65)–(66).
Update the particle stresses with the corresponding constitutive law, using the updated mechanical and thermal results.
Evolve the particle damage via Rankine's damage law.

where F is the magnitude normal line load, $R = \frac{R_1 R_2}{R_1 + R_2}$ is the equivalent body radius, where R_1, R_2 are the radii of the two contact surfaces, respectively. As the contact surface on the lower body is flat, its radius is infinite and R can be simplified as the radius of the upper contact surface. E' is the effective Young's modulus defined as: $\frac{2}{E'} = \frac{1-\nu_1^2}{E_1} + \frac{1-\nu_2^2}{E_2}$ where E_1, ν_1 and E_2, ν_2 are Young's modulus and Poisson ratio for the two contacting elastic bodies, respectively. With b, $p_{\max}$ defined, the distribution of contact pressure along the contact surface can be expressed as follows:

$$p_{cn} = -p_{\max}\sqrt{1 - (\frac{s}{b})^2} \quad \text{for } 0 \le s \le b \tag{89}$$

where p_{cn} is the contact pressure (negative in sign) and s is the distance to the center of the contact area. Since our MPM time integration is explicit, the static equilibrium solution is obtained via a dynamic relaxation method [8,102]. The vertical force applied on the top boundary (per unit width) is 156.7 N/mm. This value is substituted into (88) to determine the analytical solution on the contact surface.

We perform a mesh convergence study on this problem by discretizing the domain into three mesh sizes (size of the cells in the background grid): 0.2 mm, 0.1 mm, and 0.05 mm. The density of material points in a cell is always 4 (as a 2×2 grid) except for some cells located near the domain boundary.

We collect the contact forces on the grid nodes and use them to compute the normal contact pressure. We then compare the simulation results with the analytical solution of the normal reaction loading in Fig. 2. We observe that, the simulated contact pressure converges into the analytical pressure distribution upon consecutive mesh refinement,

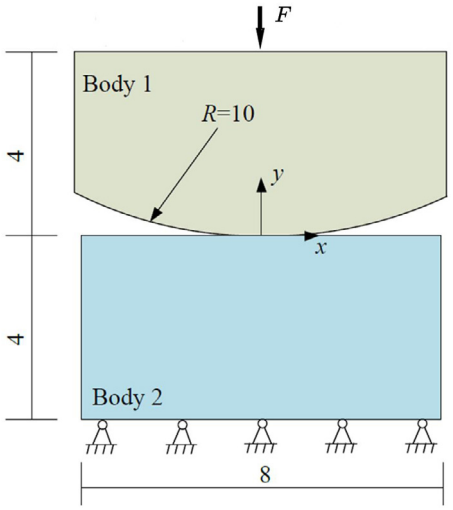

Fig. 1. Configuration for the Hertzian problem (unit in the figure is in mm).

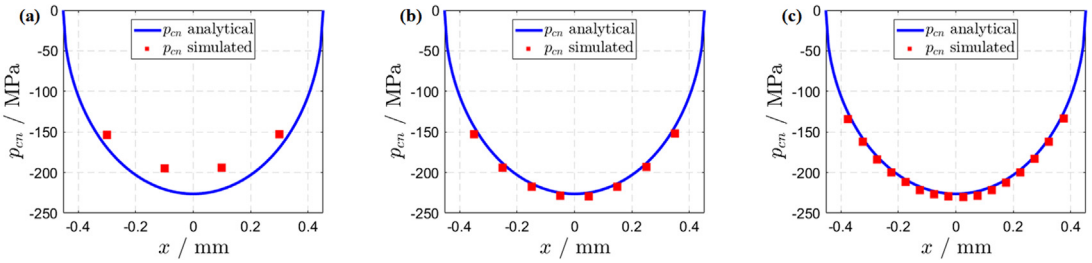

Fig. 2. Comparison of simulated contact pressure and Hertzian analytical contact pressure distribution on the contact surface. (a) mesh size 0.2 mm, (b) mesh size 0.1 mm, (c) mesh size 0.05 mm.

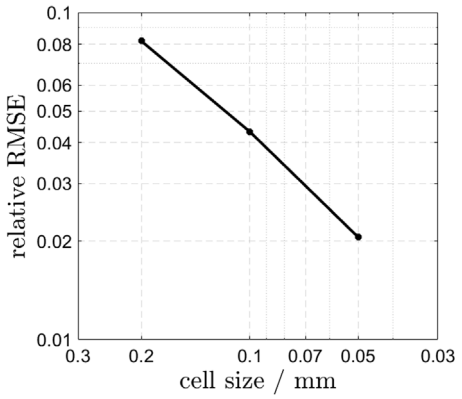

Fig. 3. Convergence of relative RMSE on the simulated contact pressures with different mesh sizes.

as indicated by the root mean square error (RMSE) of the pressure over collocation points at the contact boundary. The RMSE normalized by the maximum contact pressure is shown in Fig. 3. The stress distributions of all three cases are presented in Fig. 4, where we clearly observe a stress concentration near the contact boundary, and the maximum stress value is close to the maximum analytical contact pressure. These findings verify our approach to resolve contact problems with a gap function.

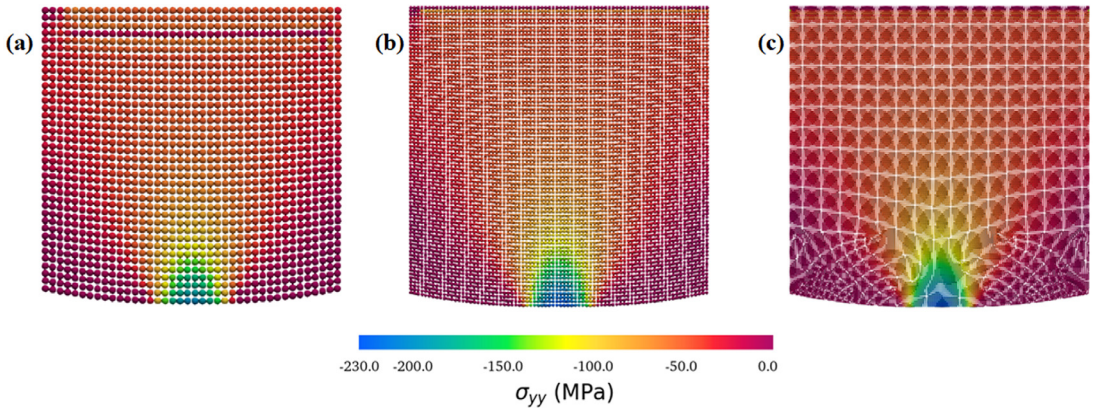

Fig. 4. Convergence study for the Hertzian contact problem with the stress contour displayed on material point clouds. (a) mesh size 0.2 mm, (b) mesh size 0.1 mm, (c) mesh size 0.05 mm.

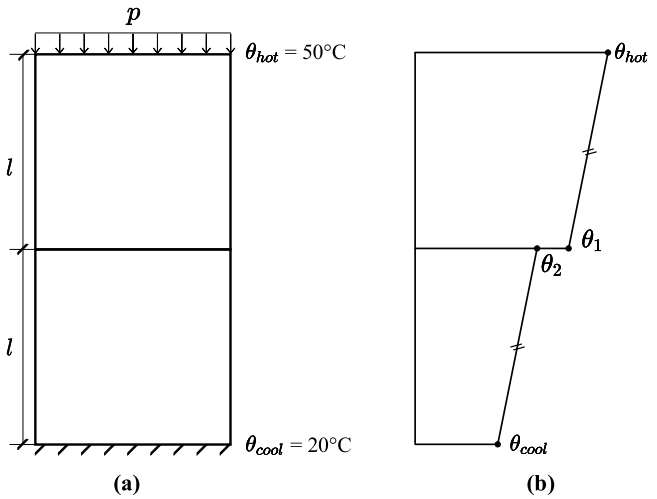

Fig. 5. Configuration of the contact heat conduction problem: (a) geometry and boundary conditions, (b) vertical profile of the steady-state temperature.

4.2. Verification against Wrigger's thermal contact benchmark problem

The purpose of this numerical example is to verify the thermo-mechanical contact MPM simulation between two contacting squared blocks subjected to both mechanical loading and thermal gradient. Previously, the same boundary value problem has been used to verify a finite element model for thermo-mechanical contact in [59]. The boundary conditions and the domain of this initial boundary value problem are shown in Fig. 5(a). The length l for both blocks is 2.5 mm and the background grid cell size is 0.5 mm. The density of material point in a cell is 4 everywhere. We fix the temperature on the top and bottom as $\theta_{\text{hot}} = 50\ ^\circ\text{C}, \theta_{\text{cool}} = 20\ ^\circ\text{C}$. A uniform pressure p is applied on the top to ensure that there is a heat transfer across the interface due to contact pressure. The motion of the lower body at the bottom is fixed. We use the same material properties for both blocks specified in Table 1, which are typical aluminum properties. The thermal expansion is ignored. This example is simulated using $\Delta t = 5 \times 10^{-8}$ s, and we specify $\zeta = 1$ so that a steady-state solution can be obtained.

The analytical solution of the temperature field along the vertical axis is piece-wise linear with a jump at the contact surface, with the specific temperature θ_1 and θ_2 for the upper and the lower body on the contact surface [cf. 59]:

$$\theta_1 = \frac{(1+\overline{\kappa}_c)\theta_{\text{hot}} + \overline{\kappa}_c\theta_{\text{cool}}}{1+2\overline{\kappa}_c} \quad , \quad \theta_2 = \frac{(1+\overline{\kappa}_c)\theta_{\text{cool}} + \overline{\kappa}_c\theta_{\text{hot}}}{1+2\overline{\kappa}_c} \quad , \quad \overline{\kappa}_c := \frac{h_c l}{\kappa}, \tag{90}$$

Table 1
Material properties (Aluminum) for the contact heat transfer verification.

Young's modulus (GPa)	E	70
Poisson's ratio	ν	0.33
Density (g/cm^3)	ρ	2.7
Specific heat (m^2/(s^{2}K))	c	900
Conductivity (N/(sK))	K	150

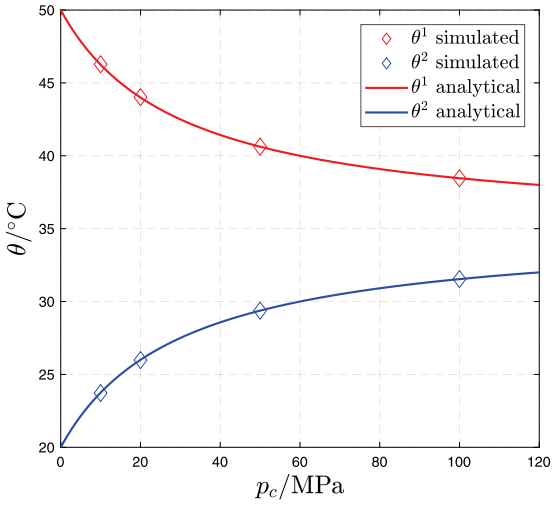

Fig. 6. Temperature at the contact surface versus the contact pressure.

where h_c is calculated from the normal contact stress (which is equal to p) with (11). As for the surface conductance coefficient $\bar{\gamma}$, we assign it with a rather large value (equals to 1) to accelerate the convergence to the steady state. The comparison between analytical results and the output from our numerical simulation is provided in Fig. 6. We observe that the stationary temperature on the two sides of the contact boundary obtained from the MPM simulation matches the analytical solutions well. This numerical example suggests that the proposed MPM is capable of simulating thermal–mechanical contacts with pressure-dependent conductance.

4.3. Validation exercise against Kalthoff–Winkler dynamic fracture experiment

The purpose of this numerical example is to validate the MPM model via an experiment reported by Kalthoff and Winkler where an edge-cracked metal plate is impacted by a projectile [103], which persists as a verification for the crack modeling with damage field in this paper. Due to the embedded symmetry of this experiment, we only model the upper half of the plate, where we set the boundary conditions at the bottom as symmetric boundary conditions. To simplify the impact loading, we assume the projectile has the same elastic impedance as the plate so that we can apply half of the impact rate as a velocity boundary condition to the surface being impacted [104]. The configuration is shown in Fig. 7. The background grid cell size is 1 mm. The cell density of material point is 4 per cell everywhere. We apply the impact load on the specimen with two velocities: 33 m/s and 100 m/s, where v_0 should be set as 16.5 m/s and 50 m/s as explained before.

The specimen is composed of steel. To utilize the Rankine damage model, we specify the critical crack energy and the critical failure stress as $G_f = 22.13$ N/mm and $\sigma_f = 570$ MPa, respectively [26]. (See Table 2).

Fig. 8 shows the results of crack propagation with applied impact velocity $v_0 = 16.5$ m/s, which corresponds to the standard impact velocity in Kalthoff and Winkler's experiments. The fracture pattern is indicated by the damage field. But according to the separation criterion in (71), fracture separation is triggered after all particles in the vicinity of a node are "fully damaged". In order to correctly retrieve the fracture propagation from such nodal information, it only matters where the damages at all associated particles are very close to 1. In this sense, we

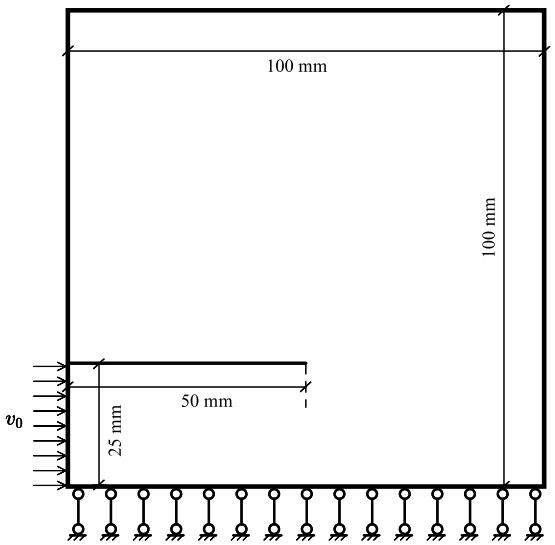

Fig. 7. Configuration of the impact fracture problem.

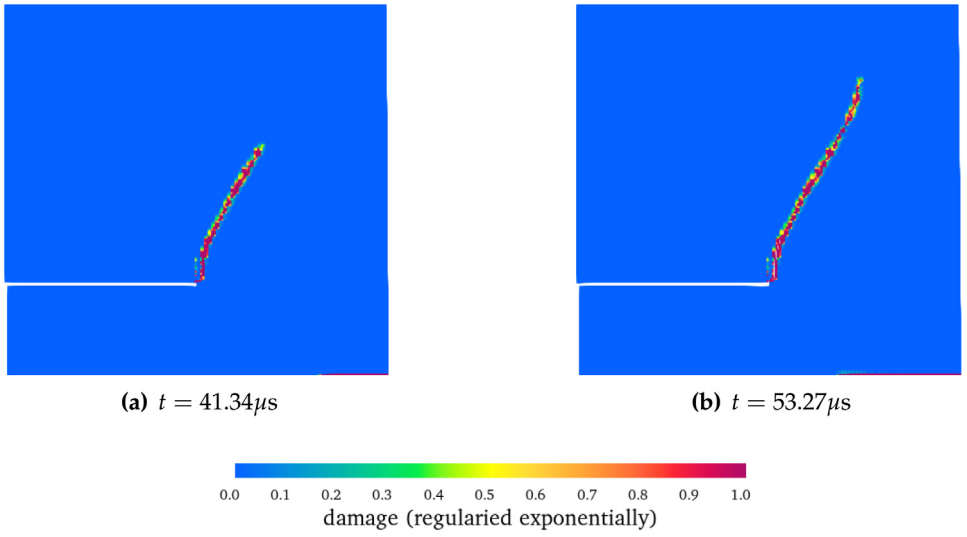

Fig. 8. Damage field at different times when impacted at 33 m/s.

Table 2
Material properties of the steel that composes the specimen used in the dynamic fracture experiment.

Young's modulus (GPa)	E	190
Poisson's ratio	ν	0.3
Density (g/cm^3)	ρ	7.8
Specific heat (m^2/(s^{2}K))	c	460
Conductivity (N/(sK))	K	55
Thermal expansion (1/K)	α	1.0×10^{-5}
Failure stress (MPa)	σ_f	570
Fracture energy (N/mm)	G_f	22.13

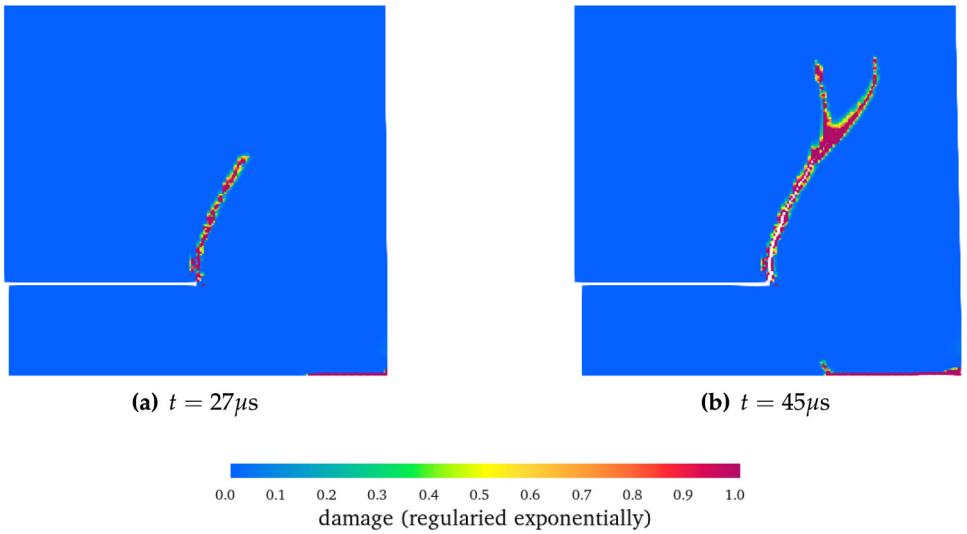

Fig. 9. Damage field at different times when impacted at 100 m/s.

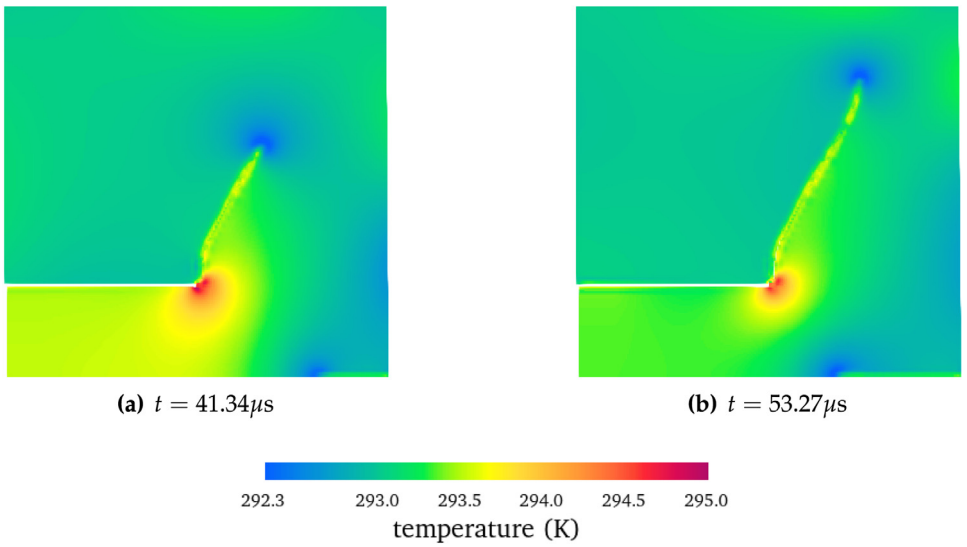

Fig. 10. Temperature field at different times when impacted at 33 m/s.

regularized the dimensionless scalar damage exponentially by $d_{\text{reg}} = (e^{5d} - 1)/(e^5 - 1)$. As shown in Fig. 8, we successfully capture a crack propagating along the direction with an angle around 67° starting at the end of the pre-notched crack, and this corresponds to the experimental results.

Apart from the standard verification problem, we are also interested in illustrating the capability of capturing complicated fracture patterns induced by fracture branching under a higher loading rate. Hence, we apply an impact velocity $v_0 = 50$ m/s and compare the simulation results with another numerical study of fracture branching in this impact fracture test. We observe that the resulting fracture pattern branches on the major tensile crack. (See Fig. 9.)

In addition to replicating crack propagation, we also investigate on the thermal response in this dynamic fracture problem. The temperature fields of both cases are shown in Figs. 10 and 11. We observe that there is a noticeable temperature increase at the lower corner of the pre-notched cracked, which is caused by stress concentration at this location and strong coupling effects. Interestingly, the crack tip cools down while the crack path behind the tip

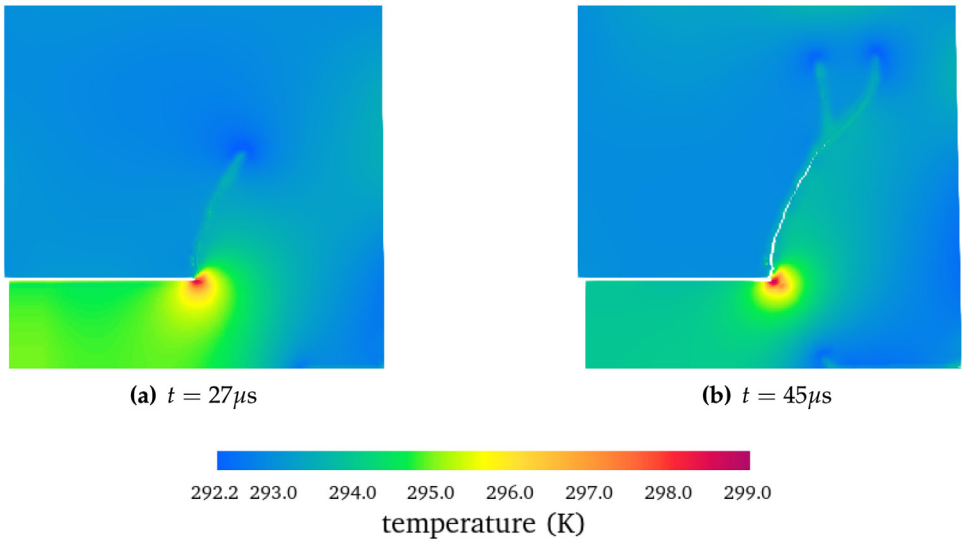

Fig. 11. Temperature field at different times when impacted at 100 m/s.

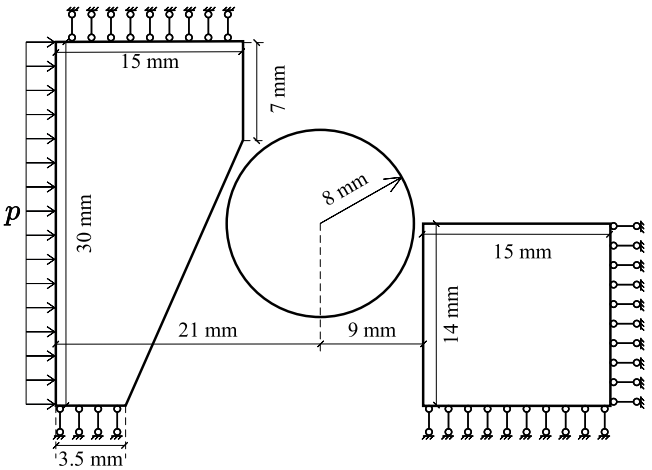

Fig. 12. Configuration of the disk squish problem.

heats up. These observations are consistent with experimental and numerical findings reported in [105] in which crack tip cooling has been observed due to the thermo-elastic cooling effect.

4.4. Thermomechanical coupling effect in dish-squish problem

In this numerical example, we adopt the "disk-squish" boundary value problem originally proposed in [26] and incorporate the thermo-mechanical coupling effect to investigate the frictional heat generated via contacts and how the friction-induced heat affects the deformation and contact evolution in return in this multi-body contact problem. The configuration is shown in Fig. 12. The cell size of the background mesh is 1 mm. The cell density of material point is always 4 per cell except for those cells adjacent to the boundaries of solid bodies. There are 2905 material points in total. The material properties are listed in Table 3, which applies to all three distinct bodies. The initial frictional contact coefficient is set as 0.4. The horizontal component of the prescribed traction p shown in Fig. 12 is 100 MPa. We use a time step of 2×10^{-8} s.

We perform a series of simulations for three different conditions: (1) isothermal conditions; (2) thermo-mechanical coupling without the thermo-mechanical softening effects on the frictional coefficient μ_c; and

Table 3
Material parameters for the disk-squish test.

Young's modulus (GPa)	E	2.25
Poisson's ratio	ν	0.125
Density (g/cm^3)	ρ	1.0
Specific heat (m^2/(s^{2}K))	c	500
Conductivity (N/(sK))	K	50
Thermal expansion (1/K)	α	1.0×10^{-5}

(3) thermo-mechanical coupling with softening on the frictional coefficient μ_c, where $\theta_{\text{dam}} = 800$ °C and $\theta_{\text{ref}} = 20$ °C. Figs. 13 and 14 show the results of both kinematic fields and thermal fields. In fact, the frictional coefficient $\mu_c = 0.4$ is sufficiently large that the body motions and x velocity distribution under both isothermal and thermo-mechanical coupling conditions are close to the non-slip contact response in [26], as shown in Fig. 13(a), (b), (c) and (d).

Comparing Fig. 13(a) and (b) with Fig. 13(c) and (d) reveals that introducing the thermo-mechanical coupling effects alone does not affect the final configuration significantly. The difference in the motions and velocity distributions of these two cases is minor. However, as shown in Fig. 14(b), the contact surface can heat up to a temperature over 900 °C due to friction and structural heating if the thermo-mechanical coupling effects are considered. If the constitutive responses of the interfaces are thermally sensitive, then the frictional heating may produce significant enough changes in the mechanical responses. This scenario is exhibited in the last simulation where the thermal softening of the frictional coefficient μ_c is considered. Fig. 13(e) and (f) demonstrate the motions and velocities of the three bodies under the conditions where μ_c decreases as temperature rises. Due to the loss of friction caused by the increased temperature, the disk in the last simulation got squeezed out of the sidewall of the rectangular body and hence the velocity of the disk is now noticeably higher in Fig. 13(f) than those exhibited in Fig. 13(b) and (d) where the friction on the contact is sufficient to prevent the sliding of the disk. These numerical simulations indicate the importance of incorporating the two-way coupling thermal–mechanical effect on the constitutive responses for the frictional contact.

As for the thermal responses, the thermal-induced reduction on frictional coefficient does lead to less heat generated at the contact. This behavior is attributed both to the difference in constitutive responses as well as the difference in the deformed geometry of the contacts affected by the constitutive responses and the two-way thermal–mechanical couplings as demonstrated in Fig. 14. Another interesting effect worth noticing is that the simulations are conducted near the adiabatic limit such that the dominated heat transfer mechanism is the convection due to the movement of the bodies. As indicated in Fig. 14, the temperature rise only takes place in few particles around the frictional contact surface, but it does not diffuse into the interior region of the bodies. Although the material is in the convection-dominated regime, the MPM framework does not trigger any spurious oscillation due to the usage of the Lagrangian description of motion for the material points.

4.5. The three-grain fragmentation problem

In this last example, we conduct a set of grains crushing simulations in a two-dimensional domain where an impact load is applied on the top of a column of three particles lumped on top of each other. This boundary value problem mimics the experiments reported in [2] but is not a direct digital replica due to the 2D idealization. Capturing the real experiments in large-scale three-dimensional simulations may require significant improvement on computational efficiency with GPU-enabled parallel computing. Such an extension will be considered in future studies but is out of the scope of this work. In this last set of numerical experiments, we conduct three simulations in which the top rigid platten are prescribed with three velocities: 8 m/s, 16 m/s, and 80 m/s, with a time step of 10^{-8} s. The simulation configuration presented by the material point cloud is shown in Fig. 15. The cell size is 0.1 mm and the density of material points in a cell is always 4 (as a 2×2 grid) except for some cells located near the domain boundary. There are 37627 material points in total. Meanwhile, the sidewalls and the bottom platten are rigid and fixed without any movement. The material properties of the three grains are identical and homogeneous. They are also typical for quartz sand (see Table 4).

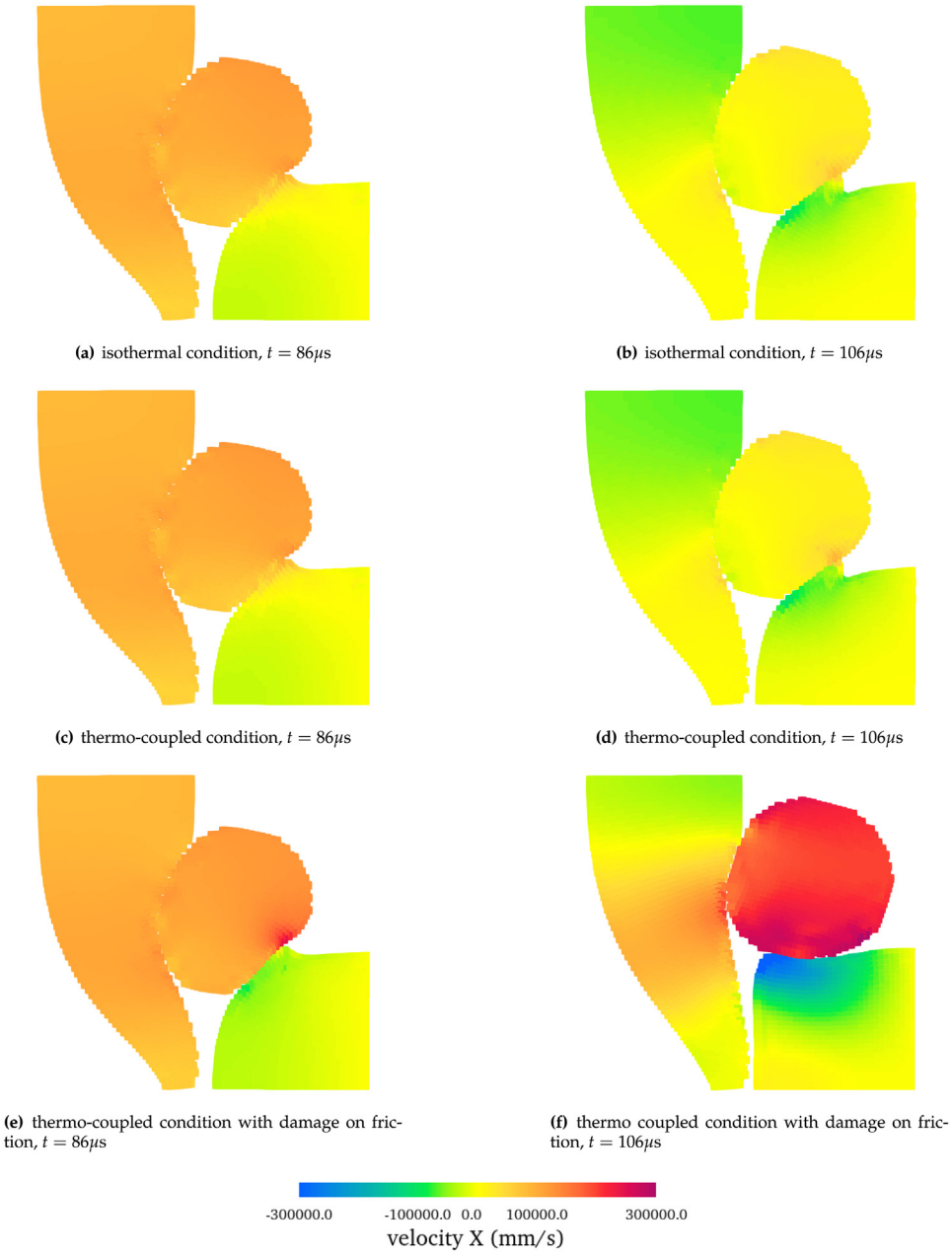

(a) isothermal condition, $t = 86\mu s$

(b) isothermal condition, $t = 106\mu s$

(c) thermo-coupled condition, $t = 86\mu s$

(d) thermo-coupled condition, $t = 106\mu s$

(e) thermo-coupled condition with damage on friction, $t = 86\mu s$

(f) thermo coupled condition with damage on friction, $t = 106\mu s$

Fig. 13. The horizontal component of the velocity field at different time steps for the isothermal case (a and b), the thermo-mechanical case without thermal-dependent friction (c and d), and the thermo-mechanical case with thermal-dependent friction (e and f).

The effects of the loading rate on the global responses can be seen in the force–displacement curve of Fig. 16. As expected, the higher loading rate triggered a larger reaction force while the slower loading rate leads to a lower peak reaction force. Nevertheless, since the granular assemblies only consist of three particles initially, an interpretation based on homogenization is not appropriate. Furthermore, due to the dynamic nature of the simulations, wave propagation within and across the particles may affect the reaction force and hence the reaction force exhibits oscillation in the temporal domain. The detailed analysis on the simulated fragmentation process, the effect of the loading rate on the evolving contacts and the thermo-mechanical responses, as well as the role of the frictional heating on the fragmentation patterns are provided in Sections 4.5.1 and 4.5.2 accordingly.

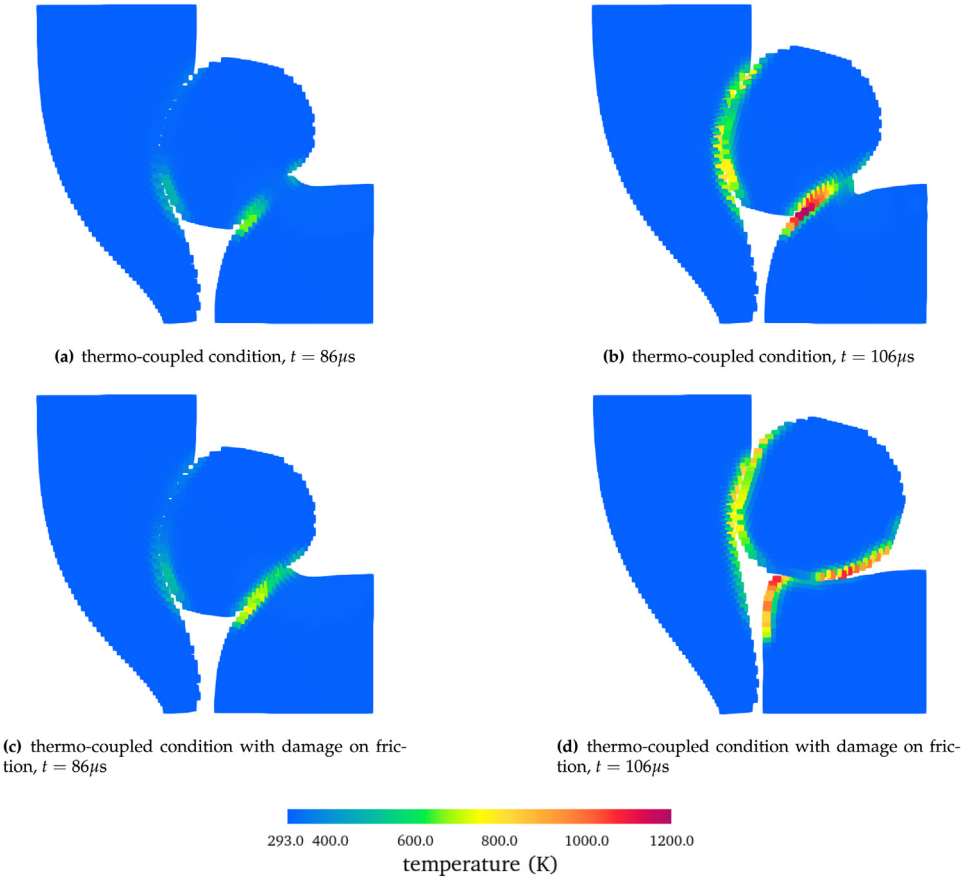

(a) thermo-coupled condition, $t = 86\mu$s

(b) thermo-coupled condition, $t = 106\mu$s

(c) thermo-coupled condition with damage on friction, $t = 86\mu$s

(d) thermo-coupled condition with damage on friction, $t = 106\mu$s

Fig. 14. Temperature distribution at different time steps for the thermal–mechanical case without thermal-dependent friction (a and b) and with thermal-dependent friction (c and d).

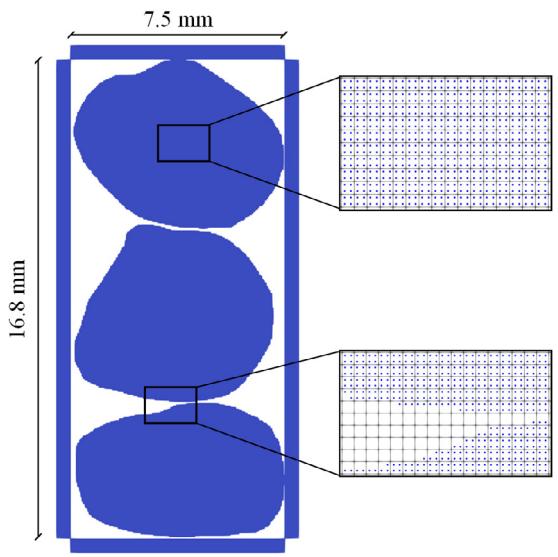

Fig. 15. Configuration for the three-grain fragmentation problem.

Table 4
Material properties typical of rock for particle crash simulation.

Young's modulus (GPa)	E	50
Poisson's ratio	ν	0.2
Density (g/cm^3)	ρ	2.3
Specific heat (m^2/(s^{2}K))	c	2000
Conductivity (N/(sK))	K	5
Thermal expansion (1/K)	α	1.0×10^{-5}
Failure stress (MPa)	σ_f	25
Fracture energy (N/mm)	G_f	0.1
Frictional coefficient at 293 K	μ_{co}	0.2

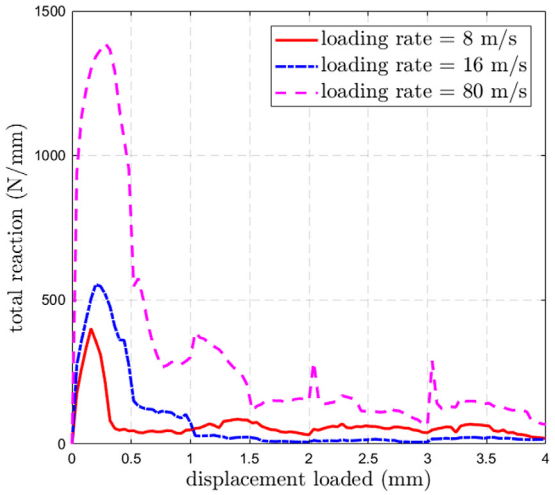

Fig. 16. Force–displacement response on the top loading platten.

4.5.1. Morphology of fragmented particles at different loading rates

As the top grain is fragmented significantly, the evolution of the topology and geometry of contacts may significantly affect the reaction force exerted on the top platten. As such, we analyze the morphology of the fragmented particles using ImageJ for all three loading cases in order to examine how impact velocity affects the dynamic fracture process. The morphological study is enabled by an open-source image analysis software called ImageJ [cf. 106]. We mask material points with $d = 1$ so that individual fragments can be distinguished from the fully crushed zones near the crack surface. For each of the three simulations of different loading rates, we analyze three snapshots of fragmentation patterns taken at selected time steps during the fragmentation process: initially cracked, fragmenting, fully crushed.

Our focus is on analyzing the probability distribution of two important geometric measures, the equivalent diameter (see Fig. 17), the diameter of a sphere (circle in 2D) that shares the same area of the fragment and the roundness (see Fig. 18), a normalized shape descriptor that measures how close the particle cross section resembles a circle, with a value of 1 indicates a perfect circle and zero indicates a line [106].

Fig. 17 shows the empirical cumulative distribution of the equivalent diameters for all three cases. This data is obtained by first identify all individual particles by identifying the boundaries of particles through image segmentation (see Figs. 19, 20, and 21). In all three cases, the impact-induced fragmentation progressively reduces the mean equivalent diameter and increases the variance of the particle size. The maximum equivalent diameter also decreases during fragmentation. These trends can be verified by the fragment pattern shown in Figs. 19, 20, and 21.

Here the top grain is initially in one piece with some initial cracks and small comminuted particles around. As the fragmentation progresses, the top grain is fragmented into smaller pieces of a variety of sizes, while the number of fragments increases significantly. This increase in the variety on particle size explains why this empirical cumulative

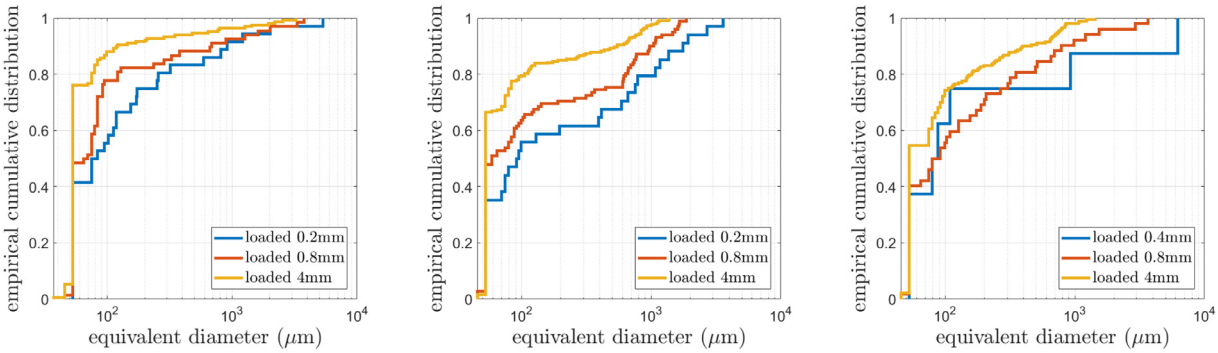

(a) loading rate 8m/s **(b)** loading rate 16m/s **(c)** loading rate 80m/s

Fig. 17. Cumulative distribution of the equivalent diameter of fragmented particles (of the top particle) for simulations with loading rates = (a) 8 m/s, (b) 16 m/s and (c) 80 m/s. The blue, red and yellow curves are obtained when the prescribed displacement on the top reaches 0.2 mm, 0.8 mm and 4 mm accordingly (except (c), see Table 4). (For interpretation of the references to color in this figure legend, the reader is referred to the web version of this article.)

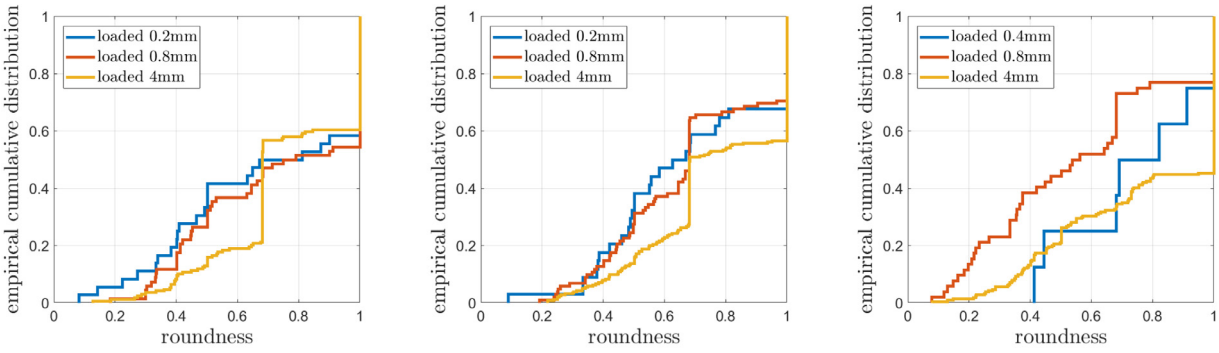

(a) loading rate 8m/s **(b)** loading rate 16m/s **(c)** loading rate 80m/s

Fig. 18. Cumulative distribution of the roundness of fragmented particles (of the top particle) for simulations with loading rates = (a) 8 m/s, (b) 16 m/s and (c) 80 m/s. The blue, red and yellow curves are obtained when the prescribed displacement on the top reaches 0.2 mm, 0.8 mm and 4 mm accordingly (except (c), see Table 4). (For interpretation of the references to color in this figure legend, the reader is referred to the web version of this article.)

distribution is smoother and more distributed as the platen moves downward. Fig. 17 also reveals that the high-speed impact tends to generate fragmentation of more distributed particle sizes. This trend may be attributed to the fact that the higher impact speed may promote crack branching. As a higher external power is supplied to the granular assembles in the case with a higher loading rate, crack branching may occur more frequently when the crack velocity reaches a threshold value [23]. As the particles split, the equivalent diameter of the new fragmented particles gets smaller than that of their "parent" particle and that further reduces the feasible length of the new crack path in the fragmented particles. Consequently, this size effect of fragmentation leads to the particle distribution becomeing increasingly well graded as the impact load is applied.

In addition to the size of fragments, we analyze the shape of fragments as well. The empirical distributions of the fragment roundness for simulations with different loading rates are shown in Fig. 18. In all three cases, the value of roundness of the fragmented particles tends to be smaller than those at the initial or fully crushed stages. This suggests that when the top grain is being fragmented starting from the initially cracked status, the newly generated fragments tend to be less rounded since the fragmentation may lead the fragmented particles with a higher aspect than the intact "parent" particle, a phenomenon also reported in [107]. However, when the fragmented particles are getting crushed further, the fragments are more rounded. This can be explained by the fact that stress concentration is more likely to occur when a sharp object is in contact with a smooth surface, which increases the probability of

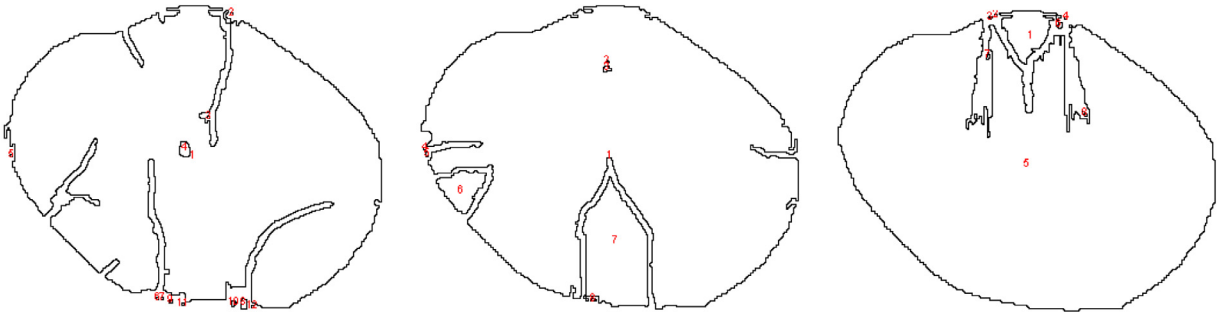

(a) loading rate 8m/s **(b)** loading rate 16m/s **(c)** loading rate 80m/s

Fig. 19. Fragment patterns in the initial cracking stage where the prescribed displacement on the top = 0.2 mm for (a) and (b) and 0.4 mm for (c).

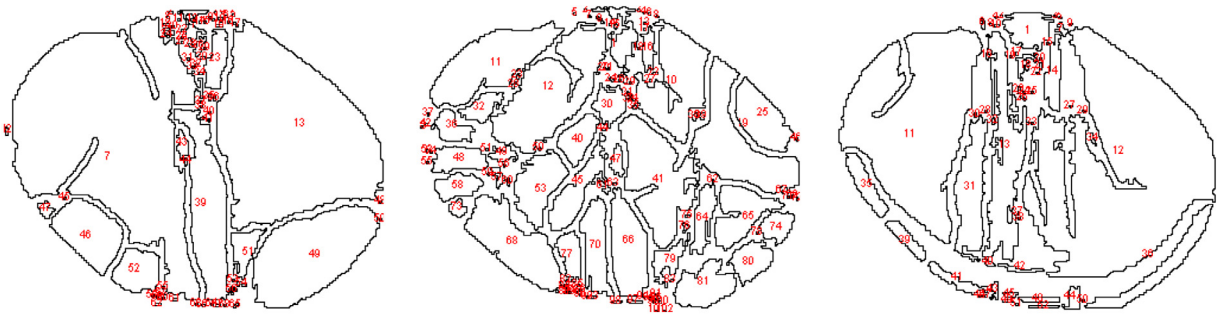

(a) loading rate 8m/s **(b)** loading rate 16m/s **(c)** loading rate 80m/s

Fig. 20. Fragment patterns after the fragmentation is triggered where the prescribed displacement on the top = 0.8 mm.

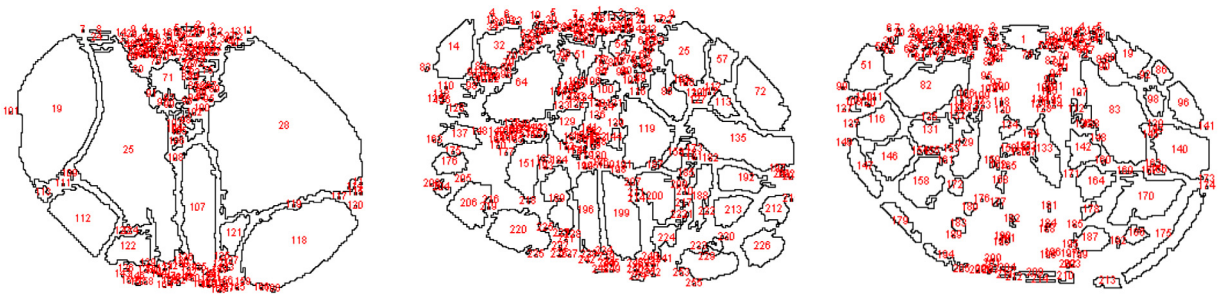

(a) loading rate 8m/s **(b)** loading rate 16m/s **(c)** loading rate 80m/s

Fig. 21. Fragment patterns when the top grain is almost fully crushed where the prescribed displacement on the top = 4 mm.

breakage into smaller and more rounded pieces for those fragments. This observation is consistent with the Weibull theory for the particle crushing process, which indicates that the survival probability of a fragmented particle under crushing is a function of the nominal tensile strength [108,109].

4.5.2. Effect of frictional and structural heating on the fragmentation

One important reason that we incorporate thermo-coupling into the mechanical formulation is to study the thermal effects involved during the fracturing process. To examine how thermo-mechanical coupling affects the fragmentation process, we introduce a control experiment where the material is assumed to remain under the isothermal condition and set the loading rate as 16 m/s. We then compare the crack pattern of the isothermal case

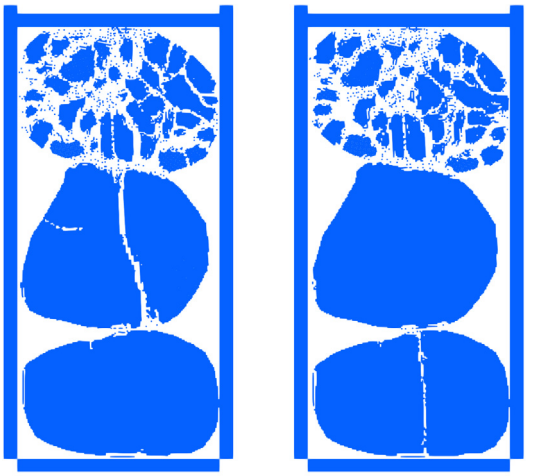

Fig. 22. Comparison of crack pattern between grain crushing simulations (a) without and (b) incorporating thermo-mechanical coupling effect. The loading rate of the top platen is 16 m/s.

and the thermo-mechanical coupling case at displacement = 16 mm in Fig. 22, where we masked fully damaged material points ($d = 1$).

Although the fragmentation pattern of the top grain looks similar, the crack pattern for the middle grain and bottom the bottom grain differs from each other significantly: in the isothermal case we observe one major vertical crack in the middle grain, but it moves to the bottom grain in the thermo-mechanical coupling case. These results indicate that crack pattern is often sensitive to perturbation and hence even the thermomechanical coupling effect with moderate temperature increase is capable of triggering a profoundly different deformed configuration. As the increased temperature reduces the frictional coefficient, and the contact stresses affect the thermal conductance of the contact, the evolution of contacts could be profoundly altered by the heat transfer and vice versa.

Note that discrete element models or level set based splitting method that uses the homogenized stress and temperature of each particle as the fragmentation criterion are incapable of replicating the interplay among the frictional contact, the heat transfer inside and across the particle, and the stress concentration at the particle contacts and hence may provide unrealistic reasons. This simplification of mechanics and geometry may have a profound effect on the interpretation of the energy scaling for the dissipated energy after the fragmentation [110,111]. Further investigations on the implication of the energy scaling using the proposed MPM framework will be considered in future studies. Figs. 23–25 show the temperature distribution in the deformed configuration for the three simulations with different loading rates. In Fig. 23, there are a few major cracks that split the top and middle particles. The crack branching around these dominating cracks is very limited. In contrast, Fig. 24 shows that the crack branching is more profound in the top grain. Those branching and diverging cracks eventually fragment the top grain into smaller pieces but there is no crack propagated into the grains at the middle and the bottom. In the last case where the impact velocity increased to 80 m/s, the region with increased temperature grows spatially due to thermal convection and no significant crack branching occur until a large portion of the prescribed displacement applied.

In all three cases, the thermal diffusivity is sufficiently low (relative to the loading rate) such that the thermal convection and the local heat caused by the damage and frictional dissipation are factors that dominate the temperature profiles. While the temperature rise in these simulations is not significant, the temperature distribution may nevertheless indicate the propagation of damage. By comparing Figs. 23–25, one may observe that the increase of the loading rate may promote crack branching and allow the heat to accumulate locally without noticeable diffusion. The crack branching may lead to a larger amount of energy dissipation at the top grain before a sufficient amount of strain energy flux causes damage in the grains at the middle and the bottom.

Note that the material could have melted if (1) the specific heat is low and/or (2) the energy dissipation is large such that the local temperature may reach the melting point without significant diffusion [112,113]. Furthermore, a more profound temperature increase may also trigger the brittle–ductile transition that affects the mechanical

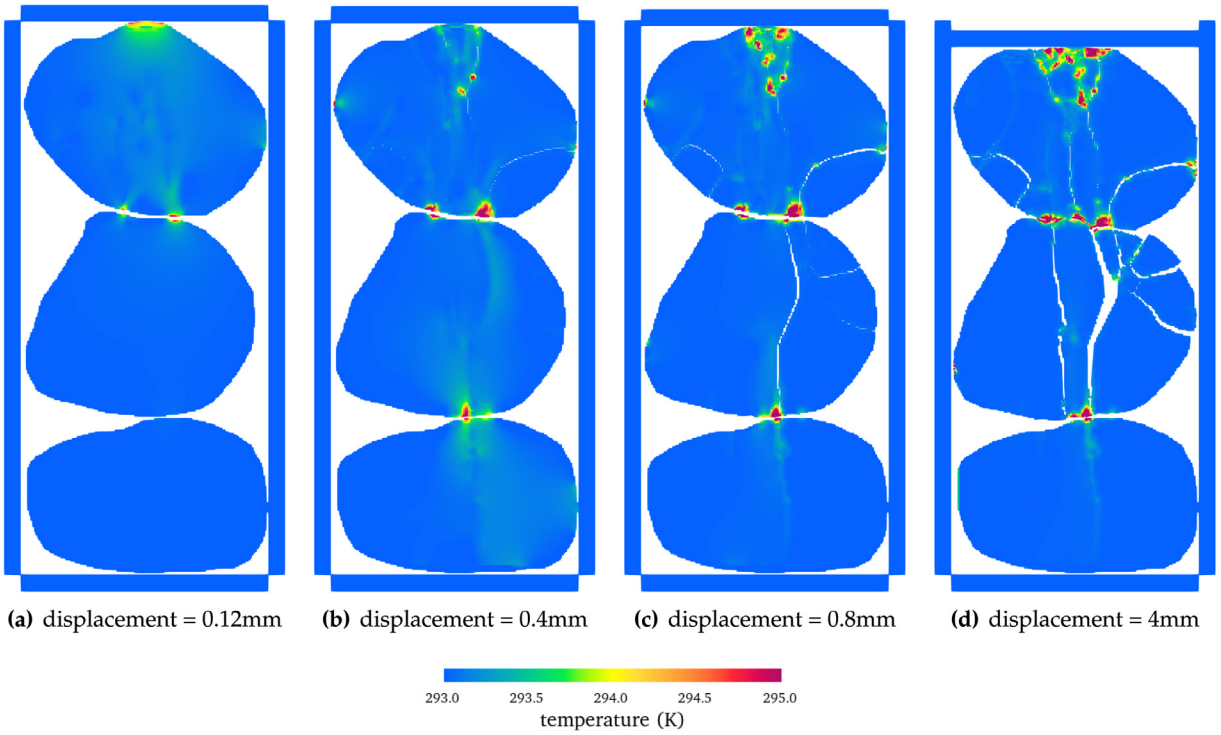

Fig. 23. Temperature field in the deformed configuration of the particles under an impact velocity of 8 m/s on the top platen.

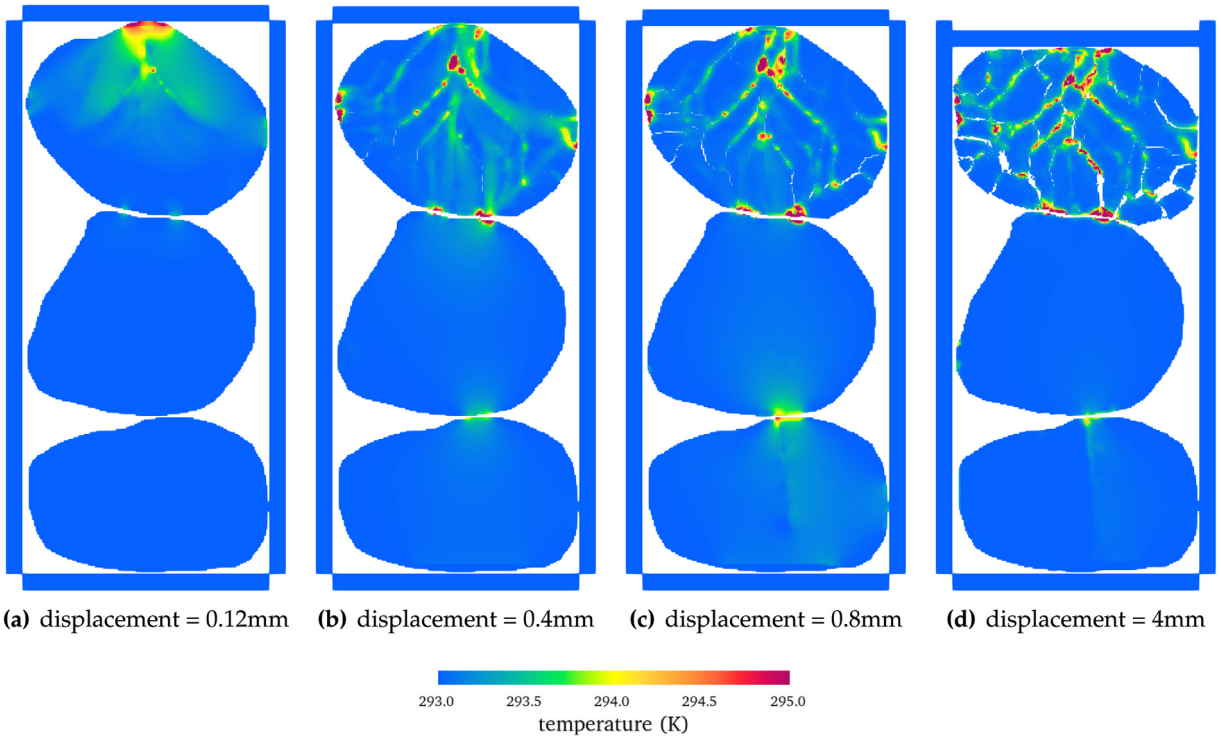

Fig. 24. Temperature field in the deformed configuration of the particles under an impact velocity of 16 m/s on the top platen.

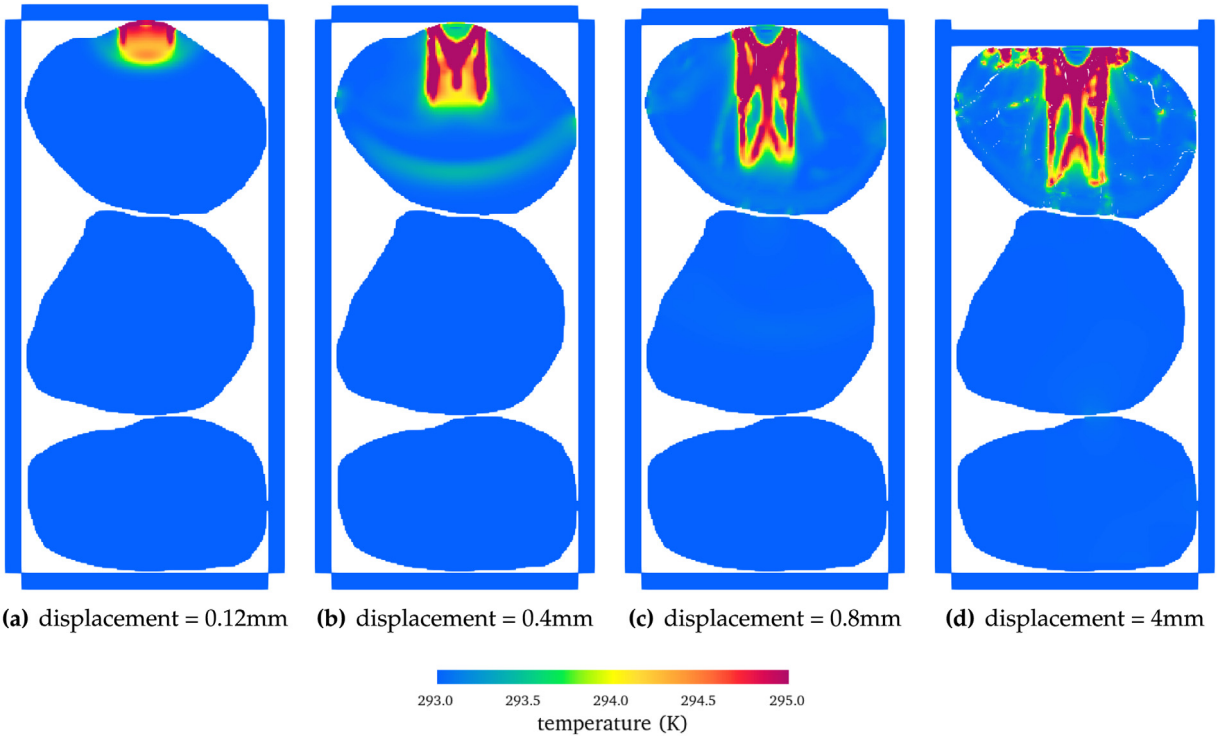

Fig. 25. Temperature field in the deformed configuration of the particles under an impact velocity of 80 m/s on the top platen.

responses and fracture patterns [43]. These mechanisms are not captured in this research but will be considered in future studies.

5. Concluding remarks

We propose a material point modeling framework designed to replicate the coupled fracture and contact mechanics under non-isothermal conditions. We incorporate a smoothed damage field gradient approach to successfully identify the field separation at potential contacting nodes while capturing the convection–diffusion of heat with Lagrangian material points. To overcome mesh sensitivity, thermal-sensitive contact and non-local damage models are used such that the degradation of the bulk material, as well as the thermal softening of the frictional interface, can both be triggered without spurious mesh dependence. We validate the resultant numerical schemes as well as use the resultant numerical models to simulate fracture and fragmentation of particle assembles with evolving contacts. Our numerical results indicate that the proposed model is capable of replicating the complex fracture patterns and the capturing the evolution of contacts under different strain rates. The role of the frictional heating on the crack growth, crack branching and the resultant fragmentation processes is analyzed.

Declaration of competing interest

The authors declare that they have no known competing financial interests or personal relationships that could have appeared to influence the work reported in this paper.

Acknowledgments

WCS is supported by the Dynamic Materials and Interactions Program from the Air Force Office of Scientific Research, United States under grant contracts FA9550-17-1-0169 and FA9550-19-1-0318, and the Earth Materials and Processes program from the US Army Research Office under grant contract W911NF-18-2-0306. MX is supported by the Presidential Fellowship of Columbia University, United States. CL's involvement is partially

supported by FA9550-19-1-0318 during his tenure as a research scientist at Columbia University, United States. These supports are gratefully acknowledged. The views and conclusions contained in this document are those of the authors, and should not be interpreted as representing the official policies, either expressed or implied, of the sponsors, including the Army Research Laboratory or the U.S. Government. The U.S. Government is authorized to reproduce and distribute reprints for Government purposes notwithstanding any copyright notation herein.

References

[1] Jiaxiang Zhang, Teng-Fong Wong, Daniel M. Davis, Micromechanics of pressure-induced grain crushing in porous rocks, J. Geophys. Res. Solid Earth 95 (B1) (1990) 341–352.
[2] M.B. Cil, K.A. Alshibli, 3D assessment of fracture of sand particles using discrete element method, Geotech. Lett. 2 (3) (2012) 161–166.
[3] SeonHong Na, WaiChing Sun, Mathew D. Ingraham, Hongkyu Yoon, Effects of spatial heterogeneity and material anisotropy on the fracture pattern and macroscopic effective toughness of mancos shale in Brazilian tests, J. Geophys. Res. Solid Earth 122 (8) (2017) 6202–6230.
[4] Chuanqi Liu, WaiChing Sun, Shift boundary material point method: An image-to-simulation workflow for solids of complex geometries undergoing large deformation, Comput. Part. Mech. 7 (2) (2020) 291–308.
[5] Chris Marone, C.H. Scholz, Particle-size distribution and microstructures within simulated fault gouge, J. Struct. Geol. 11 (7) (1989) 799–814.
[6] WaiChing Sun, Matthew R. Kuhn, John W. Rudnicki, A multiscale DEM-LBM analysis on permeability evolutions inside a dilatant shear band, Acta Geotech. 8 (5) (2013) 465–480.
[7] Matthew R. Kuhn, WaiChing Sun, Qi Wang, Stress-induced anisotropy in granular materials: Fabric, stiffness, and permeability, Acta Geotech. 10 (4) (2015) 399–419.
[8] Yang Liu, WaiChing Sun, Zifeng Yuan, Jacob Fish, A nonlocal multiscale discrete-continuum model for predicting mechanical behavior of granular materials, Internat. J. Numer. Methods Engrg. 106 (2) (2016) 129–160.
[9] Kun Wang, WaiChing Sun, Anisotropy of a tensorial Bishop's coefficient for wetted granular materials, J. Eng. Mech. 143 (3) (2017) B4015004.
[10] Ritesh Gupta, Simon Salager, Kun Wang, WaiChing Sun, Open-source support toward validating and falsifying discrete mechanics models using synthetic granular materials—Part I: Experimental tests with particles manufactured by a 3D printer, Acta Geotech. 14 (4) (2019) 923–937.
[11] Eric C. Bryant, WaiChing Sun, A micromorphically regularized Cam-clay model for capturing size-dependent anisotropy of geomaterials, Comput. Methods Appl. Mech. Engrg. 354 (2019) 56–95.
[12] Kun Wang, WaiChing Sun, Meta-modeling game for deriving theory-consistent, microstructure-based traction–separation laws via deep reinforcement learning, Comput. Methods Appl. Mech. Engrg. 346 (2019) 216–241.
[13] Kun Wang, WaiChing Sun, Qiang Du, A non-cooperative meta-modeling game for automated third-party calibrating, validating and falsifying constitutive laws with parallelized adversarial attacks, Comput. Methods Appl. Mech. Engrg. 373 (2021) 113514.
[14] Kenneth L. Johnson, One hundred years of Hertz contact, Proc. Inst. Mech. Eng. 196 (1) (1982) 363–378.
[15] Peter A. Cundall, Otto D.L. Strack, A discrete numerical model for granular assemblies, Geotechnique 29 (1) (1979) 47–65.
[16] Václav Šmilauer, Bruno Chareyre, Yade dem formulation, Yade Doc. 393 (2010).
[17] C.W. Boon, G.T. Houlsby, S. Utili, A new algorithm for contact detection between convex polygonal and polyhedral particles in the discrete element method, Comput. Geotech. 44 (2012) 73–82.
[18] Reid Kawamoto, Edward Andò, Gioacchino Viggiani, José E. Andrade, Level set discrete element method for three-dimensional computations with triaxial case study, J. Mech. Phys. Solids 91 (2016) 1–13.
[19] John M. Harmon, Daniel Arthur, José E. Andrade, Level set splitting in DEM for modeling breakage mechanics, Comput. Methods Appl. Mech. Engrg. 365 (2020) 112961.
[20] Y.P. Cheng, M.D. Bolton, Y. Nakata, Crushing and plastic deformation of soils simulated using DEM, Geotechnique 54 (2) (2004) 131–141.
[21] Baoshan Wang, Yong Chen, Teng-fong Wong, A discrete element model for the development of compaction localization in granular rock, J. Geophys. Res. Solid Earth 113 (B3) (2008).
[22] Elizabeth H. Yoffe, Lxxv. The moving griffith crack, Lond. Edinb. Dublin Philos. Mag. J. Sci. 42 (330) (1951) 739–750.
[23] J. Congleton, N.J. Fetch, Crack-branching, Phil. Mag. 16 (142) (1967) 749–760.
[24] Krishnaswa Ravi-Chandar, W.G. Knauss, An experimental investigation into dynamic fracture: III. On steady-state crack propagation and crack branching, Int. J. Fract. 26 (2) (1984) 141–154.
[25] Chuanqi Liu, WaiChing Sun, ILS-MPM: An implicit level-set-based material point method for frictional particulate contact mechanics of deformable particles, Comput. Methods Appl. Mech. Engrg. (ISSN: 0045-7825) 369 (2020) 113168, http://dx.doi.org/10.1016/j.cma.2020.113168, URL http://www.sciencedirect.com/science/article/pii/S0045782520303534.
[26] Michael A. Homel, Eric B. Herbold, Field-gradient partitioning for fracture and frictional contact in the material point method, Internat. J. Numer. Methods Engrg. 109 (7) (2017) 1013–1044.
[27] D. Rittel, L.H. Zhang, S. Osovski, The dependence of the Taylor–Quinney coefficient on the dynamic loading mode, J. Mech. Phys. Solids 107 (2017) 96–114.
[28] Aleksander Zubelewicz, Century-long Taylor-Quinney interpretation of plasticity-induced heating reexamined, Sci. Rep. 9 (1) (2019) 1–7.

[29] Charles K.C. Lieou, Curt A. Bronkhorst, Thermomechanical conversion in metals: Dislocation plasticity model evaluation of the Taylor-Quinney coefficient, Acta Mater. 202 (2021) 170–180.
[30] Jerzy L. Nowinski, Theory of Thermoelasticity with Applications, volume 3, Springer, 1978.
[31] P.X. Liu, L.Q. Liu, S.Y. Chen, G.Q. Chen, J. Ma, An experiment on the infrared radiation of surficial rocks during deformation, Seismol. Geol. 26 (3) (2004) 502–511.
[32] P.X. Liu, J. Ma, L.Q. Liu, S.L. Ma, G.Q. Chen, An experimental study on variation of thermal fields during the deformation of a compressive en echelon fault set, Prog. Natural Sci. 17 (3) (2007) 298–304.
[33] Mervyn S. Paterson, Teng-fong Wong, Experimental Rock Deformation-The Brittle Field, Springer Science & Business Media, 2005.
[34] Ted Belytschko, Robert Gracie, Giulio Ventura, A review of extended/generalized finite element methods for material modeling, Modelling Simulation Mater. Sci. Eng. 17 (4) (2009) 043001.
[35] Jens M. Melenk, Ivo Babuška, The partition of unity finite element method: Basic theory and applications, in: Research Report/Seminar für Angewandte Mathematik, vol. 1996, Eidgenössische Technische Hochschule, Seminar für Angewandte Mathematik, 1996.
[36] Arne Hillerborg, Mats Modéer, P.-E. Petersson, Analysis of crack formation and crack growth in concrete by means of fracture mechanics and finite elements, Cem. Concr. Res. 6 (6) (1976) 773–781.
[37] X.-P. Xu, Alan Needleman, Numerical simulations of fast crack growth in brittle solids, J. Mech. Phys. Solids 42 (9) (1994) 1397–1434.
[38] Francisco Armero, Christian Linder, Numerical simulation of dynamic fracture using finite elements with embedded discontinuities, Int. J. Fract. 160 (2) (2009) 119.
[39] Christian Linder, Arun Raina, A strong discontinuity approach on multiple levels to model solids at failure, Comput. Methods Appl. Mech. Engrg. 253 (2013) 558–583.
[40] Christian Linder, Francisco Armero, Finite elements with embedded branching, Finite Elem. Anal. Des. 45 (4) (2009) 280–293.
[41] Christian Miehe, Martina Hofacker, Fabian Welschinger, A phase field model for rate-independent crack propagation: Robust algorithmic implementation based on operator splits, Comput. Methods Appl. Mech. Engrg. 199 (45–48) (2010) 2765–2778.
[42] Michael J. Borden, Clemens V. Verhoosel, Michael A. Scott, Thomas J.R. Hughes, Chad M. Landis, A phase-field description of dynamic brittle fracture, Comput. Methods Appl. Mech. Engrg. 217 (2012) 77–95.
[43] Jinhyun Choo, WaiChing Sun, Coupled phase-field and plasticity modeling of geological materials: From brittle fracture to ductile flow, Comput. Methods Appl. Mech. Engrg. 330 (2018) 1–32.
[44] Eric C. Bryant, WaiChing Sun, A mixed-mode phase field fracture model in anisotropic rocks with consistent kinematics, Comput. Methods Appl. Mech. Engrg. 342 (2018) 561–584.
[45] SeonHong Na, WaiChing Sun, Computational thermomechanics of crystalline rock, Part I: A combined multi-phase-field/crystal plasticity approach for single crystal simulations, Comput. Methods Appl. Mech. Engrg. 338 (2018) 657–691.
[46] Eric C. Bryant, WaiChing Sun, Phase field modeling of frictional slip with slip weakening/strengthening under non-isothermal conditions, Comput. Methods Appl. Mech. Engrg. 375 (2021) 113557.
[47] M.G.D. Geers, R. De Borst, W.A.M. Brekelmans, R.H.J. Peerlings, Strain-based transient-gradient damage model for failure analyses, Comput. Methods Appl. Mech. Engrg. 160 (1–2) (1998) 133–153.
[48] Zdeněk P. Bažant, Milan Jirásek, Nonlocal integral formulations of plasticity and damage: Survey of progress, J. Eng. Mech. 128 (11) (2002) 1119–1149.
[49] Georgios Moutsanidis, David Kamensky, Duan Z. Zhang, Yuri Bazilevs, Christopher C. Long, Modeling strong discontinuities in the material point method using a single velocity field, Comput. Methods Appl. Mech. Engrg. 345 (2019) 584–601.
[50] Kun Zhang, Shui-Long Shen, Annan Zhou, Dynamic brittle fracture with eigenerosion enhanced material point method, Internat. J. Numer. Methods Engrg. (2020).
[51] Anna Pandolfi, Michael Ortiz, An eigenerosion approach to brittle fracture, Internat. J. Numer. Methods Engrg. 92 (8) (2012) 694–714.
[52] B. Li, Anna Pandolfi, M. Ortiz, Material-point erosion simulation of dynamic fragmentation of metals, Mech. Mater. 80 (2015) 288–297.
[53] Kun Wang, WaiChing Sun, A unified variational eigen-erosion framework for interacting brittle fractures and compaction bands in fluid-infiltrating porous media, Comput. Methods Appl. Mech. Engrg. 318 (2017) 1–32.
[54] Aurel Qinami, Eric Cushman Bryant, WaiChing Sun, Michael Kaliske, Circumventing mesh bias by r- and h-adaptive techniques for variational eigenfracture, Int. J. Fract. 220 (2) (2019) 129–142.
[55] WaiChing Sun, A stabilized finite element formulation for monolithic thermo-hydro-mechanical simulations at finite strain, Internat. J. Numer. Methods Engrg. 103 (11) (2015) 798–839.
[56] A.R. Khoei, B. Bahmani, Application of an enriched FEM technique in thermo-mechanical contact problems, Comput. Mech. 62 (5) (2018) 1127–1154.
[57] Lars Johansson, Anders Klarbring, Thermoelastic frictional contact problems: Modelling, finite element approximation and numerical realization, Comput. Methods Appl. Mech. Engrg. 105 (2) (1993) 181–210.
[58] S. Hüeber, B.I. Wohlmuth, Thermo-mechanical contact problems on non-matching meshes, Comput. Methods Appl. Mech. Engrg. 198 (15–16) (2009) 1338–1350.
[59] Peter Wriggers, Christian Miehe, Contact constraints within coupled thermomechanical analysis—A finite element model, Comput. Methods Appl. Mech. Engrg. 113 (3–4) (1994) 301–319.
[60] Daniel Pantuso, Klaus-Jürgen Bathe, Pavel A. Bouzinov, A finite element procedure for the analysis of thermo-mechanical solids in contact, Comput. Struct. 75 (6) (2000) 551–573.
[61] I. Temizer, Multiscale thermomechanical contact: Computational homogenization with isogeometric analysis, Internat. J. Numer. Methods Engrg. 97 (8) (2014) 582–607.
[62] Maik Dittmann, M. Franke, I. Temizer, C. Hesch, Isogeometric analysis and thermomechanical mortar contact problems, Comput. Methods Appl. Mech. Engrg. 274 (2014) 192–212.

[63] Alexander Seitz, Wolfgang A. Wall, Alexander Popp, A computational approach for thermo-elasto-plastic frictional contact based on a monolithic formulation using non-smooth nonlinear complementarity functions, Adv. Model. Simul. Eng. Sci. 5 (1) (2018) 5.
[64] Juan C. Simo, J.W. Ju, Strain-and stress-based continuum damage models—I. Formulation, Int. J. Solids Struct. 23 (7) (1987) 821–840.
[65] Jean Lemaitre, A continuous damage mechanics model for ductile fracture, 1985.
[66] J.C. Simo, Ch Miehe, Associative coupled thermoplasticity at finite strains: Formulation, numerical analysis and implementation, Comput. Methods Appl. Mech. Engrg. 98 (1) (1992) 41–104.
[67] J. Oliver, Continuum modelling of strong discontinuities in solid mechanics using damage models, Comput. Mech. 17 (1) (1995) 49–61.
[68] Peter Wriggers, Christian Miehe, On the treatment of contact contraints within coupled thermomechanical analysis, in: Finite Inelastic Deformations—Theory and Applications, Springer, 1992, pp. 333–347.
[69] Peter Wriggers, Giorgio Zavarise, Computational contact mechanics, Encycl. Comput. Mech. (2004).
[70] Sumio Murakami, Continuum Damage Mechanics: A Continuum Mechanics Approach to the Analysis of Damage and Fracture, volume 185, Springer Science & Business Media, 2012.
[71] Jean-Jacques Marigo, Corrado Maurini, Kim Pham, An overview of the modelling of fracture by gradient damage models, Meccanica 51 (12) (2016) 3107–3128.
[72] Jean-Louis Chaboche, Continuum damage mechanics: Part I—General concepts, 1988.
[73] A. Rieger, P. Wriggers, Adaptive methods for thermomechanical coupled contact problems, Internat. J. Numer. Methods Engrg. 59 (6) (2004) 871–894.
[74] Raymond W. Ogden, Non-Linear Elastic Deformations, Courier Corporation, 1997.
[75] Rockfield, ELFEN User's Manual, Rockfield Software Ltd., 2007.
[76] Miguel Cervera, Javier Oliyer, Rui Faria, Seismic evaluation of concrete dams via continuum damage models, Earthq. Eng. Struct. Dyn. 24 (9) (1995) 1225–1245.
[77] Miguel Cervera, Michele Chiumenti, Mesh objective tensile cracking via a local continuum damage model and a crack tracking technique, Comput. Methods Appl. Mech. Engrg. 196 (1–3) (2006) 304–320.
[78] Deborah Sulsky, Zhen Chen, Howard L. Schreyer, A particle method for history-dependent materials, Comput. Methods Appl. Mech. Engrg. 118 (1–2) (1994) 179–196.
[79] A. Gerhard Holzapfel, Nonlinear Solid Mechanics II, John Wiley & Sons, Inc., 2000.
[80] Christian Miehe, Lisa-Marie Schaenzel, Heike Ulmer, Phase field modeling of fracture in multi-physics problems. Part I. Balance of crack surface and failure criteria for brittle crack propagation in thermo-elastic solids, Comput. Methods Appl. Mech. Engrg. 294 (2015) 449–485.
[81] Jun Tao, Hongwu Zhang, Yonggang Zheng, Zhen Chen, Development of generalized interpolation material point method for simulating fully coupled thermomechanical failure evolution, Comput. Methods Appl. Mech. Engrg. 332 (2018) 325–342.
[82] Chuanqi Liu, Qicheng Sun, Gordon G.D. Zhou, Coupling of material point method and discrete element method for granular flows impacting simulations, Internat. J. Numer. Methods Engrg. 115 (2) (2018) 172–188.
[83] Alireza Sadeghirad, Rebecca M. Brannon, Jeff Burghardt, A convected particle domain interpolation technique to extend applicability of the material point method for problems involving massive deformations, Internat. J. Numer. Methods Engrg. 86 (12) (2011) 1435–1456.
[84] Ignacio Romero, Algorithms for coupled problems that preserve symmetries and the laws of thermodynamics: Part I: Monolithic integrators and their application to finite strain thermoelasticity, Comput. Methods Appl. Mech. Engrg. 199 (25–28) (2010) 1841–1858.
[85] Carlos A. Felippa, K.C. Park, Staggered transient analysis procedures for coupled mechanical systems: Formulation, Comput. Methods Appl. Mech. Engrg. 24 (1) (1980) 61–111.
[86] Charbel Farhat, Michael Lesoinne, Two efficient staggered algorithms for the serial and parallel solution of three-dimensional nonlinear transient aeroelastic problems, Comput. Methods Appl. Mech. Engrg. 182 (3–4) (2000) 499–515.
[87] Alexey Stomakhin, Craig Schroeder, Lawrence Chai, Joseph Teran, Andrew Selle, A material point method for snow simulation, ACM Trans. Graph. 32 (4) (2013) 1–10.
[88] Emmanouil G. Kakouris, Savvas P. Triantafyllou, Phase-field material point method for dynamic brittle fracture with isotropic and anisotropic surface energy, Comput. Methods Appl. Mech. Engrg. 357 (2019) 112503.
[89] Alban de Vaucorbeil, Vinh Phu Nguyen, Sina Sinaie, Jian Ying Wu, Material point method after 25 years: Theory, implementation and applications, Adv. Appl. Mech. 53 (2019) 185–398.
[90] S.G. Bardenhagen, J.E. Guilkey, K.M. Roessig, J.U. Brackbill, W.M. Witzel, J.C. Foster, An improved contact algorithm for the material point method and application to stress propagation in granular material, CMES Comput. Model. Eng. Sci. 2 (4) (2001) 509–522.
[91] John A. Nairn, Material point method calculations with explicit cracks, CMES Comput. Model. Eng. Sci. 4 (6) (2003) 649–664.
[92] Xuchen Han, Theodore F. Gast, Qi Guo, Stephanie Wang, Chenfanfu Jiang, Joseph Teran, A hybrid material point method for frictional contact with diverse materials, Proc. ACM Comput. Graph. Interact. Tech. 2 (2) (2019) 1–24.
[93] Chuanqi Liu, WaiChing Sun, ILS-MPM: An implicit level-set-based material point method for frictional particulate contact mechanics of deformable particles, Comput. Methods Appl. Mech. Engrg. 369 (2020) 113168.
[94] Tod A. Laursen, Computational Contact and Impact Mechanics: Fundamentals of Modeling Interfacial Phenomena in Nonlinear Finite Element Analysis, Springer Science & Business Media, 2013.
[95] Samila Bandara, Kenichi Soga, Coupling of soil deformation and pore fluid flow using material point method, Comput. Geotech. 63 (2015) 199–214.
[96] P. Wriggers, Ch Miehe, M. Kleiber, J.C. Simo, On the coupled thermomechanical treatment of necking problems via finite element methods, Internat. J. Numer. Methods Engrg. 33 (4) (1992) 869–883.

[97] Ines Wollny, WaiChing Sun, Michael Kaliske, A hierarchical sequential ALE poromechanics model for tire-soil-water interaction on fluid-infiltrated roads, Internat. J. Numer. Methods Engrg. 112 (8) (2017) 909–938.
[98] Hyoung Suk Suh, WaiChing Sun, Devin T. O'Connor, A phase field model for cohesive fracture in micropolar continua, Comput. Methods Appl. Mech. Engrg. 369 (2020) 113181.
[99] Hyoung Suk Suh, WaiChing Sun, An open-source fenics implementation of a phase field fracture model for micropolar continua, Int. J. Multiscale Comput. Eng. 17 (6) (2019).
[100] Heinrich Hertz, Über die berührung fester elastischer körper, J. Reine Angew. Math. 92 (156–171) (1882) 22.
[101] James R. Barber, Contact Mechanics, volume 250, Springer, 2018.
[102] Xuxin Tu, José E. Andrade, Criteria for static equilibrium in particulate mechanics computations, Internat. J. Numer. Methods Engrg. 75 (13) (2008) 1581–1606.
[103] J.F. Kalthoff, S. Winkler, Failure mode transition at high rates of shear loading, in: Impact Loading and Dynamic Behavior of Materials, vol. 1, DGM Informationsgesellschaft mbH, 1988, pp. 185–195.
[104] Jeong-Hoon Song, Hongwu Wang, Ted Belytschko, A comparative study on finite element methods for dynamic fracture, Comput. Mech. 42 (2) (2008) 239–250.
[105] O. Bougaut, D. Rittel, On crack-tip cooling during dynamic crack initiation, Int. J. Solids Struct. 38 (15) (2001) 2517–2532.
[106] Michael D. Abràmoff, Paulo J. Magalhães, Sunanda J. Ram, Image processing with imageJ, Biophotonics Int. 11 (7) (2004) 36–42.
[107] B. Zhao, J. Wang, M.R. Coop, Gioacchino Viggiani, M. Jiang, An investigation of single sand particle fracture using X-ray micro-tomography, Geotechnique 65 (8) (2015) 625–641.
[108] V.K. Voo, Statistics of Particle Strength in a Silica Sand (M. Eng. dissertation), University of Nottingham, 2000.
[109] Waloddi Weibull, et al., A statistical distribution function of wide applicability, J. Appl. Mech. 18 (3) (1951) 293–297.
[110] Zdeněk P. Bažant, Scaling laws in mechanics of failure, J. Eng. Mech. 119 (9) (1993) 1828–1844.
[111] Alberto Carpinteri, Nicola Pugno, Are scaling laws on strength of solids related to mechanics or to geometry? Nature Mater. 4 (6) (2005) 421–423.
[112] David L. Goldsby, Terry E. Tullis, Flash heating leads to low frictional strength of crustal rocks at earthquake slip rates, Science 334 (6053) (2011) 216–218.
[113] Ran Ma, WaiChing Sun, Computational thermomechanics for crystalline rock. Part II: Chemo-damage-plasticity and healing in strongly anisotropic polycrystals, Comput. Methods Appl. Mech. Engrg. 369 (2020) 113184.